Physics and Modeling of Interconnects in Printed Circuit Board Technology Considering the Attenuation and Phase Delay due to Conductor Surface Roughness

by

María Teresa Serrano Serrano

A thesis submitted in partial fulfillment of the requirements for the degree of

DOCTOR OF SCIENCE IN ELECTRONICS

at

INSTITUTO NACIONAL DE ASTROFÍSICA, ÓPTICA Y ELECTRÓNICA.

December 2023

Tonanzintla, Puebla

Advisor:

Reydezel Torres Torres, Ph., D.

Resumen

Las tarjetas de circuitos impresos (o PCBs, por sus siglas en inglés), trabajan a frecuencias de operación cada vez más altas. Por ello, el análisis de las diferentes interconexiones, así como de los materiales que los componen, se vuelve crucial para las etapas de diseño y fabricación para que cumplan con los altos requerimientos de las diversas aplicaciones de alta velocidad. Sin embargo, con el aumento de frecuencia, efectos a microescala se vuelven relevantes, afectando la propagación de las ondas electromagnéticas viajando a través de las interconexiones. La rugosidad en los conductores, es de los más importantes a tener en cuenta, ya que es añadida intencionalmente para adherir las capas de materiales conductor y de dieléctrico que dan forma a las interconexiones en PCB. Desafortunadamente, esta rugosidad aumenta considerablemente la atenuación y el retraso de las señales propagadas.

Por esta razón, en este trabajo se contribuye con el modelado de interconexiones que presenten rugosidad en los conductores, en donde se considera la relación causal entre los fenómenos físicos de atenuación y retraso asociados con la propagación de las ondas electromagnéticas. Además, se propone y se desarrolla una metodología para que, a partir de mediciones de parámetros S y de simulaciones electromagnéticas simples, se cuantifiquen las pérdidas debidas a la rugosidad en el conductor. Con esto, se puede calcular el factor de rugosidad necesario para la implementación de un modelo causal que permita describir la rugosidad presente en el conductor. Esta metodología se desarrolla primeramente en líneas de tipo microcinta, y después se propone su aplicación en antenas de parche. Posteriormente, se extiende el modelado hacia guías de onda en donde su modo de propagación sea diferente al de las líneas de microcinta. Además, también se propone una nueva ecuación para el cálculo de la impedancia de onda para guías de onda integradas en substrato (SIWs). Esta nueva formulación incluye las pérdidas debidas a los materiales y a la rugosidad presente en conductores, lo cual es una muy importante contribución para circuitos de microondas reales ya que ningún otro estudio incluye todas estas las pérdidas en el cálculo de la impedancia de SIWs.

Abstract

Printed circuit boards or PCBs are operating nowadays at increasingly higher frequencies; therefore, the analysis of the interconnects and the materials forming them is necessary. This analysis is highly recommended for the stages of design and fabrication to accomplish the requirements for high-speed applications. However, as the frequency increases, microscale effects are becoming more relevant since they significantly impact the propagation of the electromagnetic waves traveling through the interconnects. In this regard, the conductor roughness effect is one of the most important microscale effects. This is due to the fact that it is necessary to promote adhesion between the layers of conductor and dielectric materials forming the interconnects on PCBs. Unfortunately, the roughness effect significantly increases the losses and delay of the propagated signals.

For this reason, this project contributes to the modeling of interconnects exhibiting the conductor roughness effect. Besides, the causal relation between the dispersion and dissipation phenomena affecting the propagation of the electromagnetic waves, is taken into account in the modeling. Furthermore, the development of a new methodology to describe the conductor surface roughness is presented. This methodology employs S-parameter data experimentally obtained and simple electromagnetic simulations to calculate the losses and delay due to the conductor roughness effect. Once these parameters are obtained, the quantification of the roughness correction factor can be calculated and used to carry on the implementation of a causal model that physically describes the conductor surface roughness. This methodology is firstly implemented for microstrip transmission lines, but later is applied to patch antennas. Afterwards, this methodology is extended for waveguides operating at microwave frequencies with a different propagation mode. Furthermore, a new equation to calculate the wave impedance for substrate integrated waveguides or SIWs is proposed. This formulation includes the losses due to the conductor and dielectric materials, as well as the ones considering the roughness effect. This is a very important contribution for practical microwave circuits since no other study includes all these types of losses on the calculation of the wave impedance for SIWs.

Agradecimientos

Primeramente, agradezco al CONAHCyT por todo el apoyo brindado durante estos cuatro años de doctorado, y al Instituto Nacional de Astrofísica, Óptica y Electrónica por ser mi segunda casa y permitirme realizar mis estudios de posgrado.

A mi asesor, el Dr. Reydezel Torres Torres, por todo su apoyo brindado durante más de 6 años de estudios de maestría y doctorado. Gracias por su guía y su paciencia a través de un arduo camino en donde una pandemia se hizo presente. Gracias por compartirme su interés, conocimiento y experiencia en esta área de la electrónica.

A los profesores y miembros del jurado: Dr. Roberto S. Murphy Arteaga, Dr. Mario Moreno Moreno, Dr. Alfonso Torres Jacome, Dr. Alejandro Díaz Sánchez y Dra. Erika Y. Terán Bahena. Gracias por su tiempo, dedicación y contribución a la revisión de este trabajo de doctorado.

A mi familia: a mis padres y hermanos por su guía, apoyo y comprensión durante todo mi trayecto por el INAOE.

A todas las personas que conocí desde mi primer día en INAOE y que se convirtieron en compañeros y amigos durante toda esta travesía. Nunca los olvidaré.

To my family

Content

1. INTRODUCTION 9

1.1 Relevance of the conductor surface roughness on PCB technology 10

1.1.1 Physical interpretation of the conductor-related effects 10

1.1.2 Impact of resistance on attenuation 13

1.1.3 Impact of inductance on delay 14

1.1.4 Causal relation in the surface impedance components 16

1.2 Purpose of this thesis 16

2. CONDUCTOR SURFACE ROUGHNESS MODELING 18

2.1 Proposed methodology 20

2.1.1 Prototypes and experiments for proposal development 21

2.1.2 Electromagnetic simulations 23

2.1.3 Parameter extraction 25

2.2 Tests and validations 29

2.2.1 Frequency domain validation 31

2.2.2 Time domain validation 33

2.2.3 Causality test 34

2.3 Conclusions 35

3. APPLICATION OF THE SURFACE ROUGHNESS MODEL WITHIN THE W-BAND 37

3.1 Microstrip patch antenna 38

3.1.1 Structure for a microstrip antenna 38

3.1.2 Idealized design equations 39

3.1.3 Input impedance 40

3.1.4 Selection of dielectric materials 41

3.2 Separation of the microscale effects present in antennas 41

3.2.1 Antenna and microstrip prototypes and measurements 42

3.2.2 Electromagnetic simulations 45

3.2.3 Parameter extraction 47

3.3 Impact of the fiber weave effect in the performance of antennas 49

3.4 Conclusions 51

4. INCORPORATING THE SURFACE ROUGHNESS EFFECT IN THE MODELING OF SUBSTRATE INTEGRATED WAVEGUIDES 52

4.1 Approaches used for the determination of Z_{wave} 53

4.2 Relationship between γ and Z_{wave} 54

4.2.1 Development of a new expression for Z_{wave} 55

4.3 Prototypes and experiments 56

4.4 Parameter extraction 57

4.4.1 EM simulations 59

4.4 Tests and validations 60

4.5 Conclusions 63

5. GENERAL CONCLUSIONS 64

5.1 Implementation of a causal model for conductor surface roughness 64

5.1.1 Remarks on the modeling approach 64

5.2 Assessment in the performance of antennas for 5G/6G applications 65

5.2.1 Important aspects about the impact in the performance of patch antennas 66

5.3 Modeling extension to substrate integrated waveguides 67

5.3.1 Physical interpretation of the expression for Z_{wave} proposed 67

References 69

CHAPTER 1

INTRODUCTION

Since the invention of the transistor in 1947, there has been a tremendous evolution in the electronics technology. This is leading the semiconductor chips to approach physical limits while following the device density trends established by the Moore's Law [1]. Moreover, the platforms where these chips are accommodated to implement complex systems are based on printed circuit board (PCB) technology, which is also being demanded in performance to accomplish the data processing speeds required in today's applications. Therefore, the harmonics composing electromagnetic signals propagated through the corresponding interconnects fall well into the microwave frequency range; thus, the necessity of guaranteeing the signal integrity at these rates has introduced significant challenges in the modeling, characterization, and optimization of interconnects. These challenges are related to the fact that the conductor and dielectric materials constituting the interconnect interact with waves whose wavelength is comparable to the length of the guiding traces and the imperfections they present. Consequently, the microscale imperfections of the materials are 'seen' by the signal, causing losses and delay. For this reason, several R&D groups are focused on performing research for developing new and improved materials to reduce the impact of these imperfections on the electrical performance of PCBs. However, even when using these advanced materials, there are still important adverse effects at higher frequencies, which may cause considerable impact on the propagation features of the lines.

In this regard, one of the most important microscale effects degrading the signal integrity is that related to the conductor surface roughness, which increases dissipation and dispersion beyond the expected square-root-of-frequency rise stablished by the skin effect. For this reason, this phenomenon is one of the most studied on PCB technology.

Motivated by the strict requirement of accurate models for interconnects at microwave frequencies, modeling methodologies for incorporating the conductor surface roughness effect into the electrical representation of microwave interconnects are developed and experimentally verified in this project. These methodologies are based on formulations accounting for the causal relationship between the attenuation and delay associated to wave scattering

mechanisms. Using the proposed approaches, it is demonstrated, through exhaustive model–experiment correlations, that the prediction of energy absorption and dispersion in practical transmission lines on PCBs is achieved with accuracy. In fact, since the modeling presented in this project is valid for waveguides propagating signals in different modes, the application is not limited to planar lines such as microstrip and striplines, but also to rectangular waveguides such as those synthetically implemented in PCB technology (e.g., the substrate integrated waveguides or SIW). In this matter, for the first time it is presented a design equation for the wave impedance of a SIW explicitly indicating the effect of the imperfect surface roughness on its matching properties. In addition, to show the usefulness of the methodologies when designing other devices implemented with microstrip technology, the performance of patch antennas is assessed in a systematic fashion when the effects associated with the conductor are identified.

1.1 Relevance of the conductor surface roughness on PCB technology

The conductor foils that form the interconnects in multilayer PCB structures are intentionally roughened to promote adhesion with the dielectric laminates. This roughness, however, introduces peaks and valleys in the surface that act as scatterers that affect the signal propagation at microwave frequencies. In fact, any device fabricated on PCBs is susceptible to exhibit losses and delay due to this effect, which is accentuated as the operation frequency increases. This is explained hereafter.

1.1.1 Physical interpretation of the conductor-related effects

To understand the relevance of considering the conductor roughness effect in the modeling of an interconnect, it is important to picture the physical interaction of an electromagnetic field with a conductor material at microwave frequencies. Hence, the following concepts are briefly discussed to describe the context of this project.

-Skin effect:

Eddy currents originated by incident time-varying electromagnetic fields to a non-perfect conductor induce magnetic fields that reduce the magnitude of the fields into the material. This is the so-called skin effect and makes that alternating currents tend to confine in the surface of the conductor materials as signals propagate. Consider for instance a transmission line propagating signals in the quasi-transverse electromagnetic mode; for direct-current (DC) or for low-frequency operation, the current will be uniformly distributed within the cross section of the conductor traces. However, as the frequency is increased, the magnitude of the current density is higher on the periphery of the conductor since the penetration of the fields is limited by the induced eddy currents. To quantify this effect, the skin depth (δ) parameter is introduced, which is defined as the distance from the surface of a conductor material at which the current density falls to 1/*e* of its value [2], this effect is illustrated in Fig. 1.1.

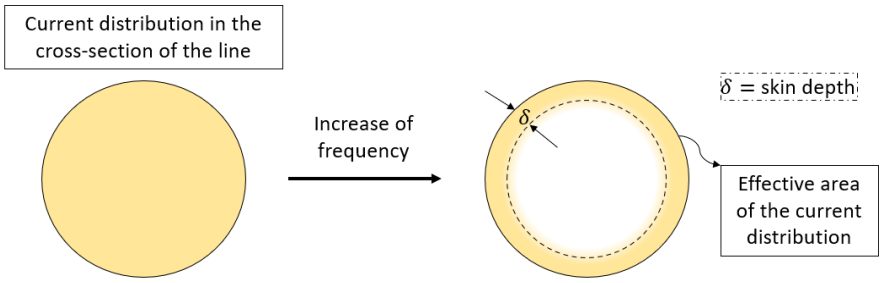

Fig. 1.1 Cross section of a cylinder wire illustrating how the current distribution changes when increasing the frequency: the current is confined to the periphery of the conductor at high frequencies.

From a practical point of view, the relevance of this effect is the substantial and frequency-dependent reduction of the area through which the current is flowing. This yields to an increase of the effective per-unit-length (P.U.L.) resistance of the line with frequency, accompanied by a reduction of its internal inductance (L_{int}). For instance, considering a microstrip transmission line of a certain width (w), and assuming that the current is confined to the bottom surface of the signal trace (i.e., where the electric field is more intense), the resistance within the current is confined in a certain area (or surface) is calculated as:

$$R_s = \sqrt{\frac{\pi\mu}{\sigma}}\frac{1}{w}\sqrt{f} = k\sqrt{f} \tag{1.1}$$

where μ is the permeability, σ is the conductivity of the material, and k is a coefficient involving the parameters μ, σ, π and $1/w$. Thus, assuming that these parameters remain approximately constant within a given bandwidth, the skin effect makes the resistance to be proportional to the square-of-root-of-frequency.

To understand the origin of this effect, it is important to say that, when the intensity of a current flowing into a conductor produces a changing magnetic field, which creates eddy currents internal in the conductor. These eddy currents will generate their own magnetic fields, and the lines of magnetic flux associated with these secondary fields point to the opposite direction [3]. Therefore, these eddy currents reduce the penetration of the magnetic field incident to the conductor surface, which indeed, physically explains the skin effect.

Since the current flows confined near the periphery of the conductor, the fields experiment the protuberances in the surface of the material due to the roughness. Furthermore, in practical PCBs, the skin depth is comparable to the feature size associated to the roughness profile. This makes evident the importance to consider the conductor surface roughness in the modeling of an interconnect such as a microstrip line, as shown in Fig. 1.2.

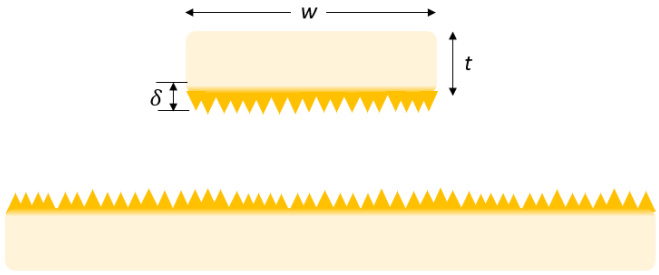

Fig. 1.2 Sketch of the cross-section corresponding to a microstrip line exhibiting roughened surface in both, the signal trace and ground plane. The dimensions of width and thickness are shown, and the current distribution is observed in the periphery of the conductors; the skin depth is also indicated.

-Internal and external inductance:

Because the skin effect modifies the current distribution within the cross section of a conductor guiding AC signals, the internal inductance of the conductor is also modified by this effect. This is the inductance associated with the opposition to a change in current due to the interaction of the magnetic fields with the conductor, and it is dependent on the properties of the conductor, its dimensions, and the frequency of operation. On the other hand, assuming quasi-TEM propagation mode, the current also forms a loop when traveling back and forth

through the signal and ground paths. This loop has associated an inductive component referred to as the external inductance (L_{ext}) [3].

The change in the current distribution due to skin effect increases the resistance, and therefore, the attenuation. In the same way, the penetration of the magnetic field into the conductor involves an increase in the delay, which is represented by means of the conductor internal inductance [4]. Furthermore, when the surface roughness effect is present in the conductor, both attenuation and delay are accentuated at frequencies of gigahertz [5].

1.1.2 Impact of resistance on attenuation

As previously mentioned, the resistance increases due to the current confinement in the surface of the conductor, which causes a loss of energy exhibited as attenuation by the conductor material. In this respect, when an electromagnetic signal is propagating through a transmission line such as a microstrip, the attenuation occurring due to interactions within the conductor material results from the joule effect. This attenuation can be mathematically expressed as [6]:

$$\alpha_c = \frac{1}{2}\frac{R_s}{\text{Re}(Z_c)} \tag{1.2}$$

where R_s is defined as in (1.1), and $\text{Re}(Z_c)$ is the real part of the characteristic impedance (Z_c). At this point, it is important to mention that equation (1.2) is valid only for a conductor with a smooth surface. However, in case the roughness of the surface is significant when compared with δ, the attenuation increases beyond the magnitude obtained from (1.2).

Lately, several models have attempted to model and quantify the increase of attenuation due to the roughness effect. Some of the first models to pay attention to this issue was the one by E. Hammerstad and O. Jensen [7], based on the S. P. Morgan approach [8]. They proposed an empirical formula to model the frequency-dependent loss through introducing a coefficient, which now allows for expressing the attenuation of a rough conductor from the attenuation of a smooth conductor as [9]:

$$\alpha_{c\_rough} = K_{HJ} \times a_c \tag{1.3}$$

where K_{HJ} is the roughness coefficient proposed by Hammerstad and Jensen, and defined as:

$$K_{HJ} = 1 + \frac{2}{\pi}\arctan\left[1.4\left(\frac{\Delta}{\delta}\right)^2\right] \tag{1.4}$$

where Δ is the root-mean-square (RMS) surface roughness feature size.

However, this model cannot represent cases with substantial surface roughness at multigigahertz frequencies. For instance, in a study made by a signaling team from Intel [9], showed the impact of the surface roughness effect and how it differs from data predicted by classical models. Fig. 1.3 illustrates part of their results, and it can be observed that the modeled curves cannot accurately represent the losses of a measured transmission line for different roughness profiles.

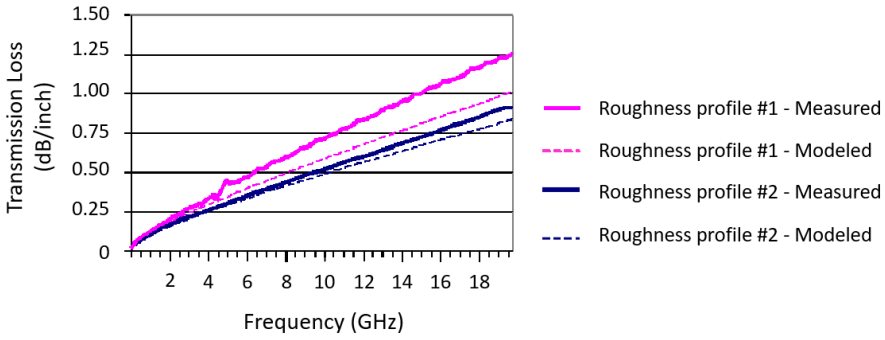

Fig. 1.3 Measured and modeled transmission loss for a practical transmission line [9].

For this reason, developments in new and improved models have emerged to counteract this issue, while respecting causality.

1.1.3 Impact of inductance on delay

The incidence of the magnetic field into a conductor material affects signal propagation in two ways. The first one is as an increase in the resistance and attenuation as previously mentioned. On the other hand, it also introduces a delay due to the existence of the internal inductance, which represents the opposition of the material to a change in the flow of an electrical current. Due to this opposition, the wave exhibits a delay when traveling through the conductor, which can be expressed in terms of the resistance and the real part of the characteristic impedance as:

$$\beta_c = \frac{1}{2}\frac{R_s}{\mathrm{Re}(Z_c)} \tag{1.5}$$

As can be seen, (1.2) and (1.5) yield to identical results when assuming a smooth surface in the conductor. However, when roughness is exhibited at the surface of the conductor, β_c increases as well. As for the case of the attenuation, β_c is related to an additional factor when the roughness parameter increases. For instance, Fig. 1.4 illustrates experimental data and the modeling for the resistance and the internal inductance associated to the attenuation and delay, respectively, increasing at different values of factors when the roughness is increased. This was recently experimentally verified [5], and it was pointed out the relevance of accounting for the effect of the surface roughness not only on the attenuation, but also on the phase delay. In Fig. 1.4 these effects are represented by means of the resistance and internal inductance, respectively.

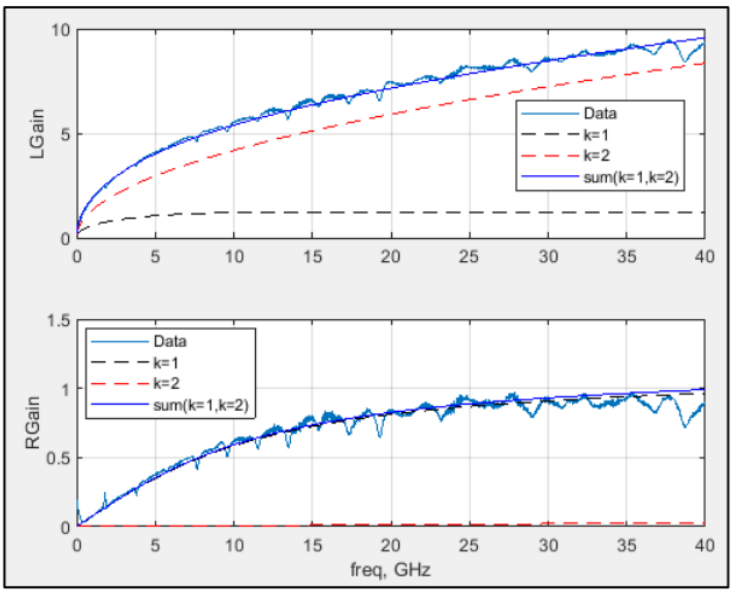

Fig. 1.4 Increase of the internal inductance (top), and resistance (bottom), due to surface roughness [5].

As can be seen in Fig. 1.4, the resistance *R* and the inductance *L* increase at different rates, for this reason, it is necessary to consider different roughness factors for these parameters. Furthermore, it is worthwhile mentioning that these factors are linked through causality, as explain hereafter.

1.1.4 Causal relation in the surface impedance components

When the current is confined at the surface of the conductor due to the skin effect at high frequencies, it can be assumed that the current is flowing in a laminar form. In this case, the properties of the conductor can be represented using the concept of 'surface impedance' (Z_s). In fact, the surface impedance is a complex function where its real part is associated to the resistance, and the imaginary part is associated to the internal inductance, as expressed in the following formulation:

$$Z_s = R_s + X_L \tag{1.6}$$

where R_s is the surface resistance defined as in (1.1), and X_L is the inductive reactance, defined as $X_L = 2\pi f L_{int}$. With this formulation, it is confirmed that the skin effect simultaneously causes a decrease in the inductance while increasing the resistive losses, implying a causal relationship between the energy stored and the energy dissipated by the conductor [10].

However, as previously explained, R and L_{int} change at different rates when considering the conductor surface roughness. For this reason, several models for incorporating the impact of the rough surface on the attenuation are typically formulated with the aid of the complex surface impedance, for instance, the well-known P. G. Huray's 'snowball' model [11]. Unfortunately, this model requires the obtention of L_{int} through the total line's inductance, which is not always straightforward. Furthermore, other models based on the determination of Z_s, require either the topological description of the conductor rough surface, or the accurate value of Z_s, which are not always available. To counteract this part, this project provides solutions based entirely on data corresponding to the electrical response of interconnects.

1.2 Purpose of this thesis

This work contributes to the modeling of the roughness effect by taking into consideration the causal relation between the phenomena of dispersion and dissipation effects. This enables the quantification of the losses and delay due to the conductor surface roughness for different interconnects and devices in PCBs. Furthermore, the roughness factors for the attenuation and delay are quantified and the implementation of a causal model for the conductor surface roughness effect is performed for microstrip transmission lines. Also, the application of the

methodology used for microstrip lines is applied to patch antennas. Finally, the modeling is extended to waveguides fabricated in PCB technology, which operate in a different propagation mode than the microstrip lines. This extension assures the application of the modeling in different types of transmission lines.

CHAPTER 2

CONDUCTOR SURFACE ROUGHNESS MODELING

Planar interconnects on PCB and particularly microstrip lines are fundamental elements in electronics packaging technology. Thus, delay and loss effects occurring in these structures should be accurately analyzed for understanding the corresponding impact on signal propagation. And even at some tens of gigahertz, radiation of energy in microstrip PCB lines represents less than 5% of the total signal loss in practical applications [12]. Hence, the losses related to the interaction of electromagnetic waves with conductor and dielectric media are those mainly affecting the performance of these lines [13]. In this regard, it is important to separate the contributions of these two interactions in order to develop a full model that can be incorporated into a simulation tool. With this motivation, the contribution presented in this work is the characterization and modeling of the conductor-related delay and loss in actual microstrip interconnects. For this purpose, experimental *S*-parameters and electromagnetic (EM) simulations are used in a systematic fashion to allow for its straightforward application by PCB designers and for R&D groups dedicated to develop new and improved materials.

However, when experimentally determining electrical parameters, the first challenge to be faced is that several phenomena are involved in the response of a system. Hence, to develop modeling techniques for either conductor or dielectric related effects, it is necessary to first identify each one of these effects in measured data. This is explained in the present chapter, as well as the characterization and modeling of the frequency-dependent effects happening when a microwave signal interacts with conductors in a practical circuit.

Based on this discussion, one of the main contributions of this thesis is the development and implementation of a causal model for conductor surface roughness; as well as demonstrating its application for the representation of microstrip lines with different surface profiles. Also, a brief summary of the models used to account for the roughness effect in conductors will be reviewed.

To begin with, the conductor foils are intentionally roughened to promote adherence between the dielectric and conductive layers when building multi-layer circuits. In typical high-

speed circuits, this process is obtained through standard electro-deposition of copper (STD) or reverse treated electro-deposition (RTF) [14], [15]. However, an adverse effect of this roughness is that the attenuation of signals (i.e., α = Re(γ)) is increased beyond the typical square-root-of-frequency trend imposed by the skin effect.

For this reason, several approaches have been proposed to account for the corresponding loss in models for α on rough conductor materials. One of the most popular is that related to the 'snowball' (also called 'cannonball') model proposed by Paul Huray, et al. [11]. This model proposes the use of multiple spheres of different radii to describe the topography of a rough conductor surface, as can be seen in Fig. 2.1. This representation accurately predicts the scattering of the electromagnetic fields and its effect on the electrical characteristics of the lines. In fact, it shows superiority when comparing the results with those obtained through traditional approaches based on the Samuel P. Morgan concept of pyramids [8], which is the basis of the well-known model by E. Hammerstad and O. Jensen [7].

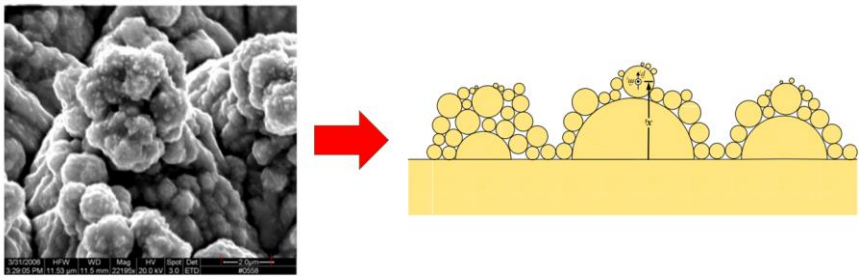

Fig. 2.1 Photograph (left) showing the detail of the surface of a copper foil used on PCB technology, and a sketch (right) illustrating how the corresponding protuberances are represented using the 'snowball' concept [11].

However, the implementation of models based on the topographic features of the metal foils requires detailed information of the surface, commonly obtained through optical measurements. Furthermore, the causal relation between the effects of dissipation and dispersion tends to be ignored when modeling the conductor roughness effect. To overcome the foretold limitation of these models, J. Bracken proposed a causal modeling using Huray's approximation [16]. Later, a second approach was made by L. Simonovich et al [17], where a complex correction factor was proposed to quantify the increase in α and β when the surface roughness effect was present in the materials [17]. For this purpose, rather than using an arbitrary number of spheres of different radii to construct the unit cell to represent the surface profile, a 14-sphere array of equal radius was proposed. In this case, a 'cannonball' pyramidal

structure is used to describe an effective roughened surface. To implement this model, only one parameter is needed: the peak-to-valley height parameter (R_z), which is directly related to the radius of the sphere, allowing the characterization of the surface profile. The problem is that still measurements of the profile are needed, or alternatively, R_z is obtained through curve fitting, increasing the possibility of losing the physical significance of the model parameters.

Hence, in this thesis an equation is proposed to determine the roughness parameter R_z without the need to perform optical measurements. Here, electrical experiments, complemented by electromagnetic simulations under idealized conditions are used as part of the extraction for R_z. This is a new methodology where the determination of the contributions for the conductor and the dielectric materials is achieved. For this reason, the procedure allowing the implementation of a causal roughness model for microstrip lines is fully described in this chapter.

2.1 Proposed methodology

As previously mentioned, microstrip lines present signal attenuation mainly due to three types of losses attributed to: the joule effect in the conductor, polarization currents in the dielectric, and radiation [12]. For all practical purposes, on PCB technology at frequencies up to some tens of gigahertz, the latter can be ignored since its magnitude is relatively small [18]. Therefore, the dominant losses in microstrip lines are the ones due to the conductor and to the dielectric materials. In fact, since lines on PCB exhibit noticeable but low loss, it is possible to assume that the phase delay (β = Im(γ)) is much larger than α [13]. This in turn allows for expressing the total attenuation as the sum of the conductor and dielectric attenuations (i.e., α_c and α_d, respectively); mathematically:

$$\alpha \approx \alpha_c + \alpha_d \tag{2.1}$$

Similarly, the phase delay exhibits contributions from the conductor and dielectric materials, respectively represented by β_c and β_d. Hence, under the low-loss transmission line assumption, is possible to write:

$$\beta \approx \beta_c + \beta_d \tag{2.2}$$

However, the experimental determination of the conductor and dielectric contributions on both α and β considering the surface roughness effect is cumbersome. This is due to the fact that the

functions describing the frequency dependent effects associated to these two media are similar. Bear in mind also that performing electromagnetic simulations considering the microstrip structure including the metal surface roughness is not an option due to the small size of the protuberances (i.e., the structure is large and the mesh for accounting the imperfect profile is fine). For this reason, the following methodology is proposed:

1. Performing electromagnetic simulations assuming perfect conductors are used to determine the dielectric contribution on both α and β.
2. Combining electromagnetic simulations and experimental data determining α and β associated to the conductor effects.
3. Calculation of the versus-frequency roughness correction factor for α, allowing the determination of the sphere radius (r) through a quadratic regression. Once r is known, R_z can also be identified.
4. Comparison of results with optical measurements to validate the proposed equation. These measurements are independently obtained, not required during the application of the proposal, and just used for verification purposes.
5. Through simulations using the proposed model implementation, the quantification of the attenuation and phase delay due to conductor losses is performed.
6. Validation of the methodology in the frequency and time domains.
7. Causality testing.

These steps will be explained in the following subsections.

2.1.1 Prototypes and experiments for proposal development

To develop the methodology, microstrip transmission lines with two different lengths (l_1 = 25 mm and l_2 = 320 mm) and four widths (w_1 = 230 µm, w_2 = 255 µm, w_3 = 330 µm and w_4 = 355 µm) were fabricated specifically to analyze the impact of the conductor effects; the lines were built with copper with a thickness of t = 35 µm over a dielectric laminate with height h = 127 µm. For this purpose, the Isola's Tachyon 100G laminate with a nominal relative permittivity and loss tangent of $\varepsilon_r = 2$ and $\tan\delta = 0.002$, respectively, was employed. Also, three different prototypes were fabricated; these prototypes exhibit the same characteristics with the exception of the copper surface roughness profiles (R_z = 1, 2, and 3 µm). During fabrication, the foils were mechanically adhered to the dielectric laminate prior to final annealing, which avoids significant change in the surface profile. This fabrication step is not applied in practice but it is important here to validate the proposal when comparing the results obtained from electrical

experiments with those corresponding to optical measurements. To provide further information about the prototype, a cross-section sketch of the microstrip lines, without considering the surface roughness, is shown in Fig. 2.2.

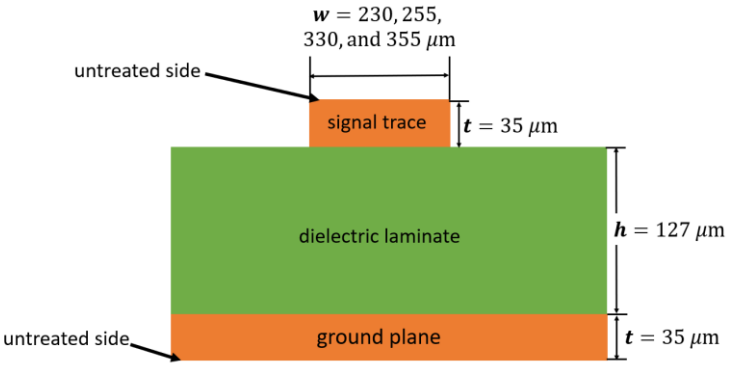

Fig. 2.2 Cross-section of the microstrip line prototypes detailing the dimensions without considering the roughness profiles.

After fabrication, these prototypes were measured in the high-frequency laboratory of INAOE using a measurement setup including a vector network analyzer (VNA), coaxial cables and general precision coaxial connectors (GPC) [19]. These connectors helped in the minimization of standing waves and mitigating radiation effects. The measurement frequency range spans from 100 MHz up to 35 GHz. For illustration purposes, Fig. 2.3 shows the measurement setup including the lines attached to the connectors and then, to the VNA port 1 and 2.

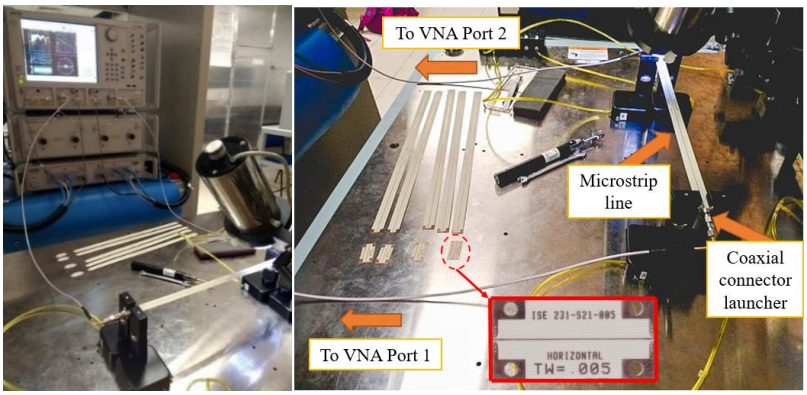

Fig. 2.3 Photographs of the High-Frequency Laboratory of INAOE, demonstrating the setup for measurement, and the microstrip line prototypes. The inset in the right photograph shows one of the shortest prototyped microstrip lines.

Once the *S*-parameters were obtained, they were processed using the line-to-line algorithm [20]. This allows to obtain the per-unit-length (P.U.L.) α and β free of the effect of the coaxial

connectors. In this regard, Fig. 2.4 shows the propagation constant curves for a specific width case (w_1 = 230 µm), obtained through this method and for all the available surface profiles. As expected, a noticeable increase in the attenuation was observed when rising R_z. However, in the curves for the phase delay, this effect is evidenced only when calculating the group delay as:

$$\tau_g = \partial\beta/\partial\omega \tag{2.3}$$

where $\omega = 2\pi f$ is the angular frequency.

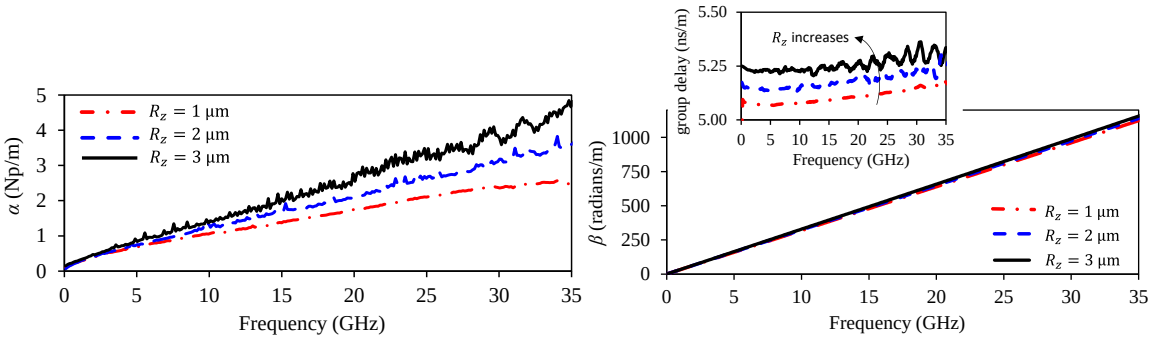

(a) (b)

Fig. 2.4 Curves obtained from experimental γ for a microstrip line of a fixed width and different surface profiles: (a) attenuation, and (b) phase delay with an inset showing the increase of the group delay when R_z increases.

2.1.2 Electromagnetic simulations

To separate the effects determining α and β, performing EM simulations was initially proposed under the idealized condition of perfect conductors, and assuming only dielectric losses ($\tan\delta = 0.002$) This allows determining the dielectric-related α_d^{EMS} and β_d^{EMS}; where the 'EMS' superscript indicates that these parameters were obtained from an EM simulation.

For the case of α, to obtain the conductor losses including the roughness effect (i.e., $\alpha_{c\_\mathrm{rough}}$) from experimental α and simulations, (2.1) is rewritten as:

$$\alpha_{c\_\mathrm{rough}} = \alpha - \alpha_d^{\mathrm{EMS}} \tag{2.4}$$

For β, a similar procedure is followed. However, in this case, it is important to remark that the conductor surface roughness reduces the height of the dielectric material [21], causing a change in the effective permittivity experienced by a signal propagating through the line [22].

Therefore, to properly consider this effect on β, the following equation to calculate the effective height of the dielectric laminate is applied:

$$h_{eff} \approx h - R_{z\_\mathrm{MS}} - R_{z\_\mathrm{G}} \tag{2.5}$$

where R_{z_MS} and R_{z_G} are the roughness features of the microstrip and ground surfaces, respectively; for these prototypes, $R_{z\_\mathrm{MS}} = R_{z\_\mathrm{G}}$. Once h_{eff} is considered in the EM simulation and assuming the idealized conditions already mentioned, (2.2) can be rewritten to obtain the phase delay due to conductor roughness effect (β_{c_rough}) from experimental β as:

$$\beta_{c\_\mathrm{rough}} = \beta - \beta_d^{\mathrm{EMS}} \tag{2.6}$$

To illustrate the importance of considering h_{eff}, Fig. 2.5 shows three different scenarios where an overestimation in β_{c_rough} is observed when the change in height in the dielectric material is not considered.

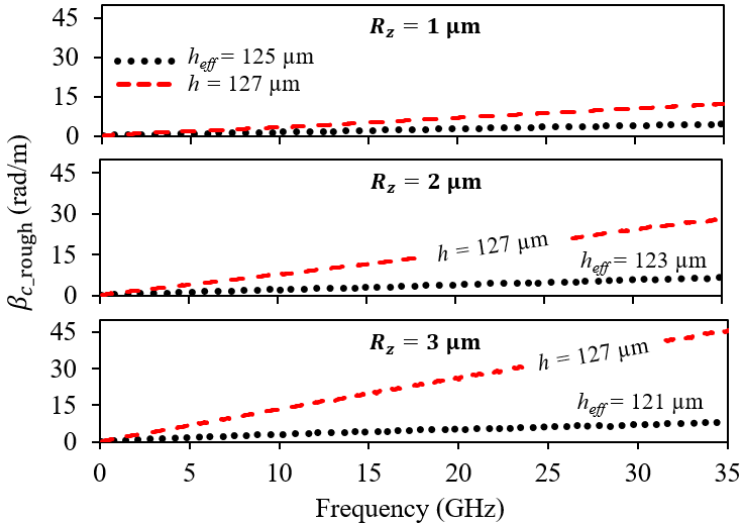

Fig. 2.5 β_{c_rough} curves obtained for different profiles, calculating the change in height due to the presence of surface roughness and when it is not considered.

From Fig. 2.5, it can be concluded that an accurate implementation of the model will not be possible when ignoring the change in the effective dielectric height due to the surface roughness. Consequently, it is important to properly account for this effect in the phase delay.

2.1.3 Parameter extraction

The next step before implementing the causal model is calculating the complex correction factor introduced by the imperfect conductor surface. This factor is the one that allows for considering the increase in magnitude in α and β beyond the square-root-of-frequency function associated to the skin effect. For the case of the attenuation, K_α is defined and calculated as in [23]:

$$K_\alpha = \alpha_{c\_\text{rough}}/\alpha_{c\_\text{smooth}} \tag{2.7}$$

where α_{c_smooth} is the attenuation when assuming that the microstrip line is made with smooth conductors, and can be calculated through a simple EM simulation or as in [3]:

$$\alpha_{c\_\text{smooth}} \approx \frac{K_s\sqrt{f}}{2Z_{qs}} \tag{2.8}$$

where Z_{qs} is the line's characteristic impedance using a quasi-static calculation, whereas K_s is the smooth conductor surface resistance given by [24]:

$$K_s \approx 1/w\sqrt{\pi\mu_0/\sigma} \tag{2.9}$$

where w is the width of the line, μ_0 is the vacuum permeability, and σ is the bulk conductivity.

On the other hand, modeling the phase delay also requires to consider a correction factor introduced by the conductor roughness (i.e., K_β) and is linked to K_α through causality. Therefore, as for the case of the attenuation, K_β can be defined as:

$$K_\beta = \beta_{c\_\text{rough}}/\beta_{c\_\text{smooth}} \tag{2.10}$$

where $\beta_{c\_\text{smooth}} = \alpha_{c\_\text{smooth}}$ can be assumed since the resistive and reactive components of a smooth conductor present the same magnitude [25]. This was verified by performing two different simulations for the microstrip lines considering smooth conductors. For the first one, actual copper was assumed, which allows determining α_{c_smooth}. The second one was made assuming perfect conductors. Hence, the second simulation does not include the effect of β_{c_smooth}, and this parameter can then be obtained by a subtraction of the betas of these two simulations. This results in barely distinguishable curves as shown in Fig. 2.6.

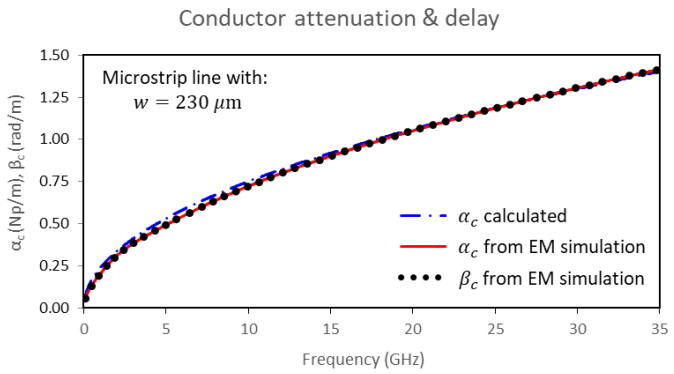

Fig. 2.6 Simulated α_{c_smooth} and β_{c_smooth} curves for a microstrip line assuming perfectly smooth conductors.

At this point, versus-frequency data for the roughness correction factors can be obtained from (2.7) and (2.10). Hence, the next step is using models to reproduce these data. For this purpose, the correction factors for the attenuation and phase delay are respectively defined as in [17]:

$$K_{\alpha\_\text{model}} = 1 + \frac{(\Delta K - 1)c_x f}{c_x f + \sqrt{2c_x f} + 1} \tag{2.11}$$

$$K_{\beta\_\text{model}} = 1 + \frac{(\Delta K - 1)\,(c_x f + \sqrt{2c_x f})}{c_x f + \sqrt{2c_x f} + 1} \tag{2.12}$$

These equations are obtained after carrying out an analysis based on the 'snowball' approach, but assuming that the metal profile can be described using cells consisting of 14 spheres of fixed radius (r). In this case, it is obtained that $\Delta K \approx 8.33$ [26], and $c_x = 2\pi\mu_0\sigma r^2$.

In (2.11) and (2.12), only one parameter is unknown, c_x. Therefore, since K_α from the experimental results is known from (2.7), c_x can be obtained rewriting (2.11) as a quadratic regression:

$$y - 1/2c_x = \left(x + 1/\sqrt{2c_x}\right)^2 \tag{2.13}$$

where $y = (\Delta K - 1)f/(K_\alpha - 1)$ and $x = \sqrt{f}$. In this case, (2.13) represents a parabola with vertex in $(-1/\sqrt{2c_x}, 1/2c_x)$. In this regard, Fig 2.7 shows the data from experiment calculated as in (2.7), and the quadratic fit using (2.13), where it is also given the cases when there is an underestimation and an overestimation for r. The illustrated case corresponds to a microstrip line with w = 230 µm and R_z = 3 µm.

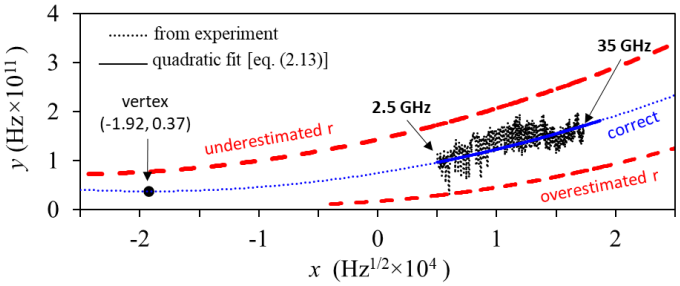

Fig. 2.7 Quadratic regression applied to experimental data to obtain c_x in the model for the surface correction factors.

When c_x is known through the regression proposed in (2.13), r can be calculated from:

$$r = \sqrt{2\pi\mu_0\sigma/c_x} \tag{2.14}$$

whereas R_z can be obtained from [17]:

$$R_z = r/0.06 \tag{2.15}$$

Fig. 2.8 summarizes the results for r for the different available widths obtained when applying the proposal and when using profile measurements of the copper foils employed during the fabrication of the prototypes.

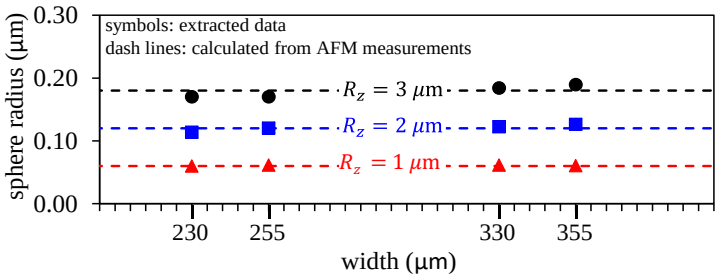

Fig. 2.8 Estimation of r for all the widths and profiles available in the prototypes.

The results for R_z shown in Fig. 2.8 include those obtained from an atomic force microscopy (AFM) measurement. This confirms that using a regression including experimental data gives the same magnitude for the R_z parameter, as that from actual topography measurements of the conductor. In this way, it is proved that this methodology presents the advantage of avoiding the requirement of a-priori knowledge of R_z.

Now, since r and R_z are known, (2.11) and (2.12) can be calculated, and $\alpha_{c\_\mathrm{rough}}$ and β_{c_rough} can be rearranged as:

$$\alpha_{c\_\mathrm{rough}} = K_{\alpha\_\mathrm{model}} \times \alpha_{c\_\mathrm{smooth}} \tag{2.16}$$

$$\beta_{c\_\mathrm{rough}} = K_{\beta\_\mathrm{model}} \times \alpha_{c\_\mathrm{smooth}} \tag{2.17}$$

At this point, the correlation between the model using (2.16) and (2.17), and experimental data using (2.4) and (2.6), is shown for the attenuation case in Fig. 2.9, and for the phase delay case in Fig. 2.10. These comparisons are made for all the available widths and roughness profiles.

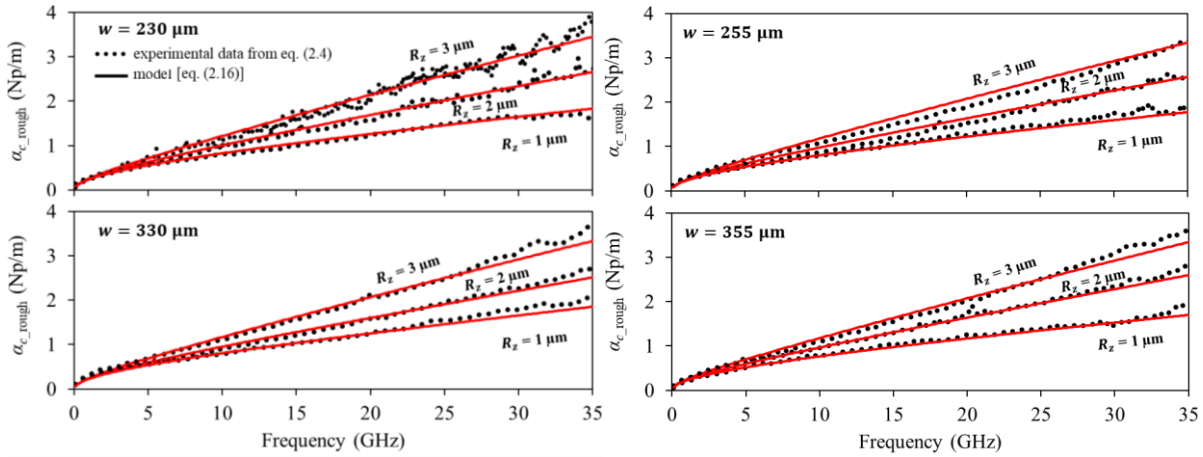

Fig. 2.9 Conductor attenuation curves for the lines of different widths and copper profiles, showing an agreement between the model used and experimental data.

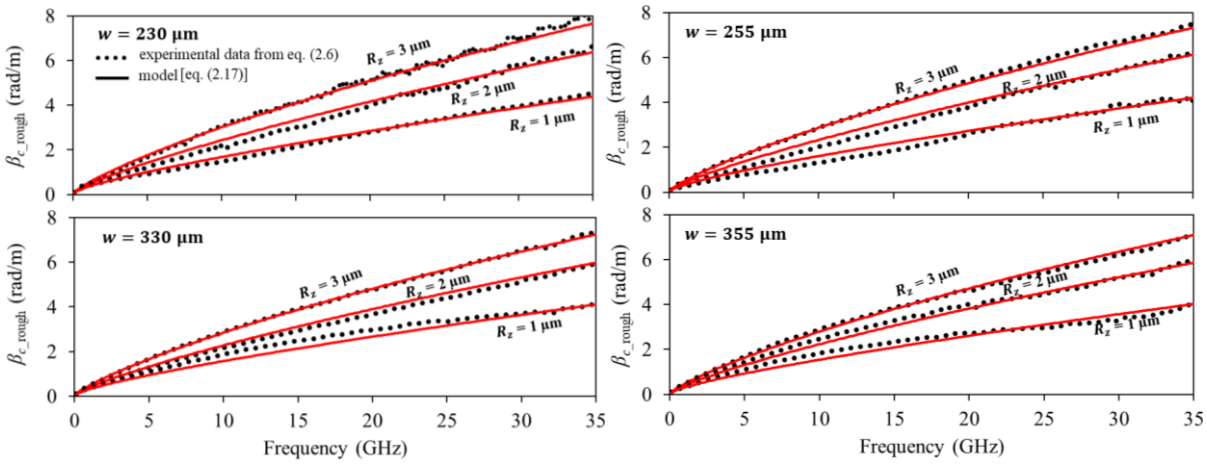

Fig. 2.10 Phase delay curves including the conductor effect. All the roughness profiles and widths considered in the prototypes are shown.

To conclude this section, the parameter extraction methodology is summarized in the flowchart of Fig. 2.11.

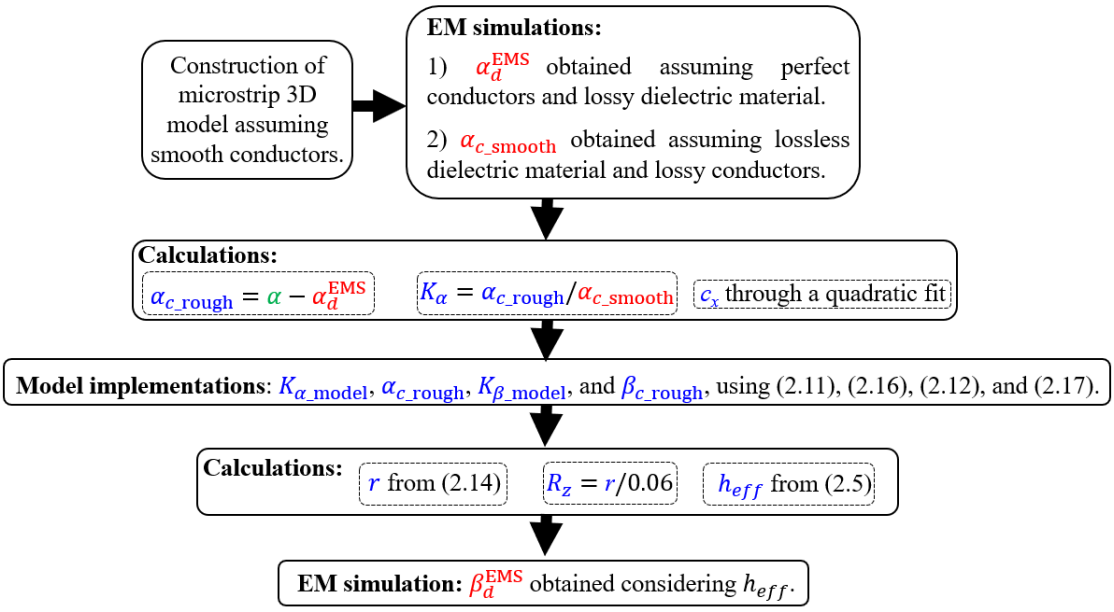

Fig. 2.11 Flowchart illustrating the methodology followed for the implementation of a causal model for surface roughness in microstrip lines.

2.2 Tests and validations

To complete the validation of the modeling technique shown here, K_α and K_β were plotted in Fig. 2.1. From this figure, it was concluded that the common assumption used in previous models of $K_\alpha = K_\beta$, is not correct since $K_\beta > K_\alpha$ was observed. Therefore, the roughness effect in the phase delay cannot be neglected in the propagation features of transmission lines, as previously predicted in [27].

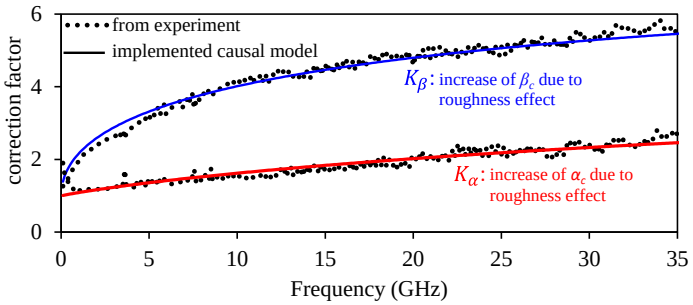

Fig. 2.12 Correction factors for the attenuation and phase delay for a case of a microstrip line with w = 230 µm and R_z = 3 µm.

To further observe the effect of the conductor roughness in β, the phase velocity was calculated as:

$$v_p = \omega/(\beta_c + \beta_d) \tag{2.18}$$

where β was split into the contributions of the conductor and dielectric materials to quantitatively analyze the impact in each material. Therefore, to only assess the change in the phase velocity due to the conductor, the following equation was applied:

$$v_p^c = \frac{\omega}{K_\beta \beta_{c\_\text{smooth}} + \omega/c} \tag{2.19}$$

where c is the speed of light in vacuum. In this case, it is assumed that the microstrip line is surrounded by free-space and $K_\beta \beta_{c\_\text{smooth}} = \beta_c$ and $\omega/c = \beta_d$ are substituted into (2.18).

On the other hand, the phase velocity affected only by the dielectric material is assumed when $\beta_c = 0$, yielding to:

$$v_p^d = \omega/\beta_d \tag{2.20}$$

In this manner, Fig. 2.13 shows how the phase velocity changes because of either the conductor or dielectric materials and even when smooth and roughened surfaces are assumed. To ease the reading of these graphs, the curves are normalized to the speed of light in vacuum.

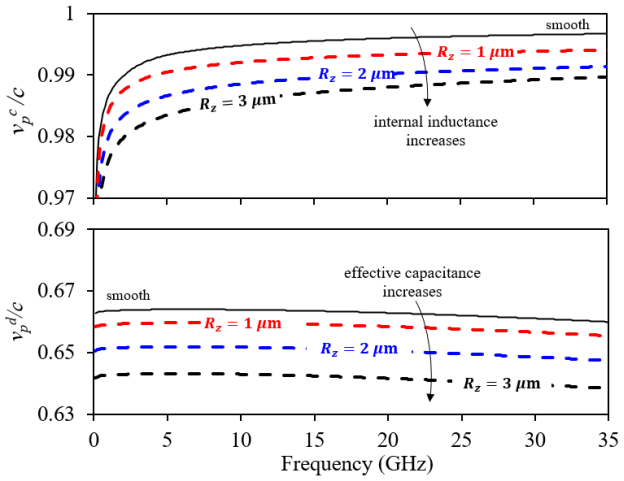

Fig. 2.13 Phase velocity curves normalized to the speed of light in vacuum observing a reduction due to the roughness effect on the conductor (top) and on the dielectric (bottom).

From Fig. 2.13, it was confirmed that the conductor roughness impacts the signal interaction with both the conductor and the dielectric materials; thus, affecting in two different ways: a

change in the internal inductance of the conductor, and a change in the effective capacitance and effective permittivity of the dielectric media (i.e., the combination of the PCB dielectric laminate and air) experienced by the propagating signal.

2.2.1 Frequency domain validation

To assess the influence of the roughness effect on the characteristic impedance (Z_c) when the roughness effect is present in the microstrip line, Z_c was calculated as:

$$Z_c = \frac{R + j\omega L}{\alpha_c + \alpha_d + j(\beta_c + \beta_d)} \tag{2.21}$$

where, again, α and β were separated into their conductor and dielectric contributions. Furthermore, α_c and β_c are calculated using the previous results from the modeling considering that the parameter R_z is already known, and α_d and β_d are obtained from EM simulations. While R and L are the per-unit-length resistance and inductance, respectively, and are given by:

$$R = K_\alpha K_s \sqrt{f} \tag{2.22}$$

and

$$L = L_{\text{ext}} + L_{\text{int}} \tag{2.23}$$

where L_{ext} is taken from an EM simulation under the perfect conductor condition, and:

$$L_{\text{int}} = \frac{K_\beta K_s}{2\pi\sqrt{f}} \tag{2.24}$$

Therefore, the calculations for Z_c were made considering three different cases:

1. Using the causal model (where $K_\alpha \neq K_\beta$)
2. Non-causal assumption (where $K_\alpha = K_\beta$), and
3. Ignoring β_c (i.e., $K_\beta = 0$)

These results are shown in Fig. 2.14 for a microstrip line of w = 230 μm and for all the roughness profiles, using (2.21)-(2.24).

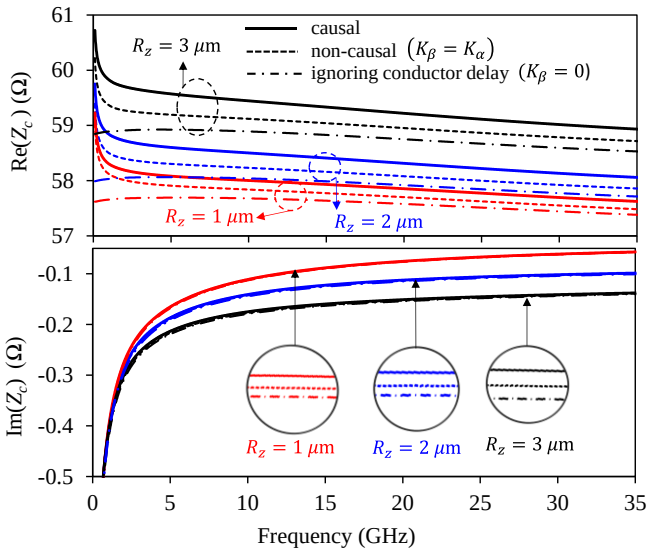

Fig. 2.14 Real and imaginary parts of the characteristic impedance applying the causal model and when simplifications are considered.

Using Z_c, and α and β for a given length, ABCD-parameters where firstly calculated and then converted to *S*-parameters. Using his approach, the *S*-parameters were reconstructed using the same three assumptions already mentioned. Then, the insertion loss (i.e., $|S_{21}|$) was obtained for a fixed length and width, for all the surface profiles. In Fig. 2.15(a), it was observed a good model-experiment correlation for S_{21}. While in Fig. 2.15(b), the group delay for the phase of S_{21} is presented, also showing a good agreement between model and experiment.

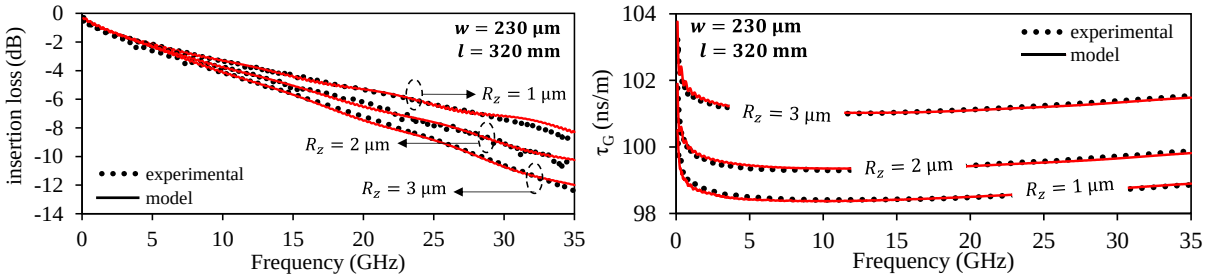

(a) (b)

Fig. 2.15 Curves showing the (a) insertion loss, and (b) the group delay for the phase of S_{21}, illustrating a good agreement between the experimental data and model.

2.2.2 Time domain validation

For using frequency domain data to perform time domain simulations of a linear system, the low frequency response should be known. Unfortunately, microwave VNAs are not capable of measuring under DC conditions. For this reason, here an extrapolation to low frequencies considering among other parameters, the resistance calculated under direct-current (DC) conditions was carried out. This was achieved by calculating the value of the resistance at DC frequency and mathematically incorporating it to the reconstructed *S*-parameters.

In Fig. 2.16(a), the P.U.L. resistance versus frequency curve is shown for a microstrip line width of w = 230 µm presented up to 35 GHz. While in Fig. 2.17(b), a zoomed-in picture of the P.U.L. resistance is shown including the value of the DC resistance, and the extrapolation data to zero frequency.

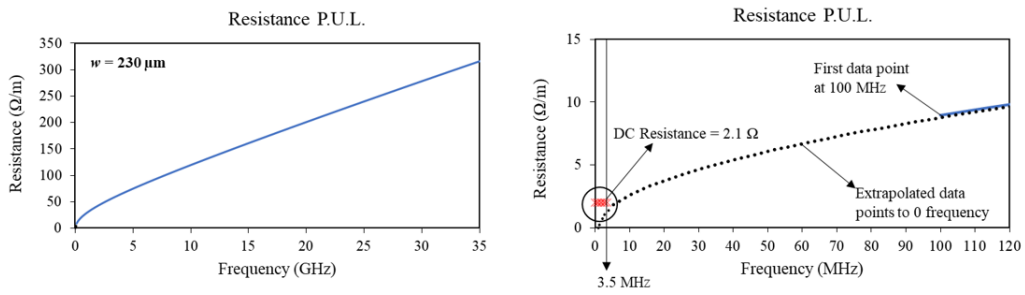

(a) (b)

Fig. 2.16 P.U.L. Resistance shown in (a) when the whole frequency range is considered, and (b) zoom-in illustrating extrapolated points at DC frequencies.

Once the DC resistance is known and included in the *S*-parameter data, inverse Fast Fourier Transform (iFFT) was used to determine time domain results. In this manner, the curves for the transmitted voltage along a line of length of 320 mm and for all the R_z height-parameter available were obtained, as shown in Fig. 2.17. The time domain simulations were performed using a pulse voltage with equal rise and fall edges of 29 ps and a pulse width of 1V of 50 ps. Furthermore, the previous analyzed cases when the conditions of causal and non-causal modeling, and ignoring conductor delay were assumed, are considered as well for these simulations. In this case, the longest line was chosen to remark the differences between the three cases. Also, a bigger time delay was observed when R_z was increased.

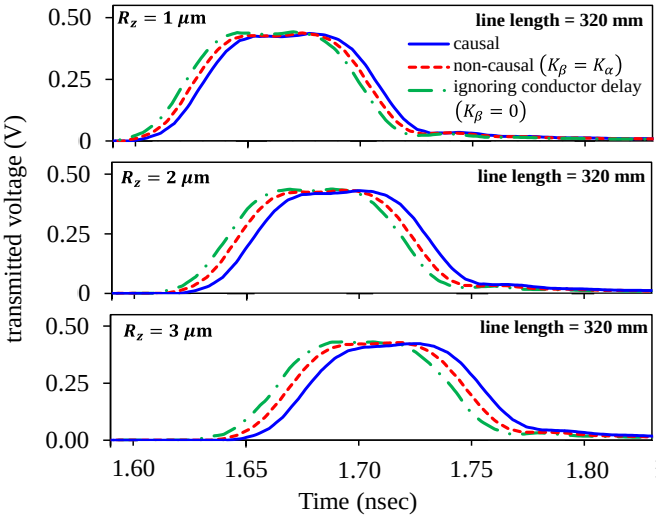

Fig. 2.17 Curves for the transmitted voltage when applying the causal model and when common simplifications are considered. The illustrated case corresponds to a line of length l = 320 mm and for all the available profiles.

2.2.3 Causality test

To verify that the corresponding time response is zero before any stimulus is happening [28], a test for causality must be applied. This test is performed in the frequency domain once the reconstructed *S*-parameter data are obtained. The procedure consists in generating tabular data for the real parts of the *S*-parameters, afterwards, the corresponding imaginary parts are computed by considering the so-called dispersion relations with subtractions [29]. This allows to define the lower and upper bounds within which the model curves must fall [30]. In this regard, Keysight's ADS circuit simulator allows to check for causality for the *S*-parameter data by defining a threshold, and following the methodology previously described. Fig. 2.18 shows the real and imaginary part for the return loss (i.e., S_{11}) and the insertion loss for a line with characteristics of R_z = 3 μm, w = 230 μm and l = 25 mm.

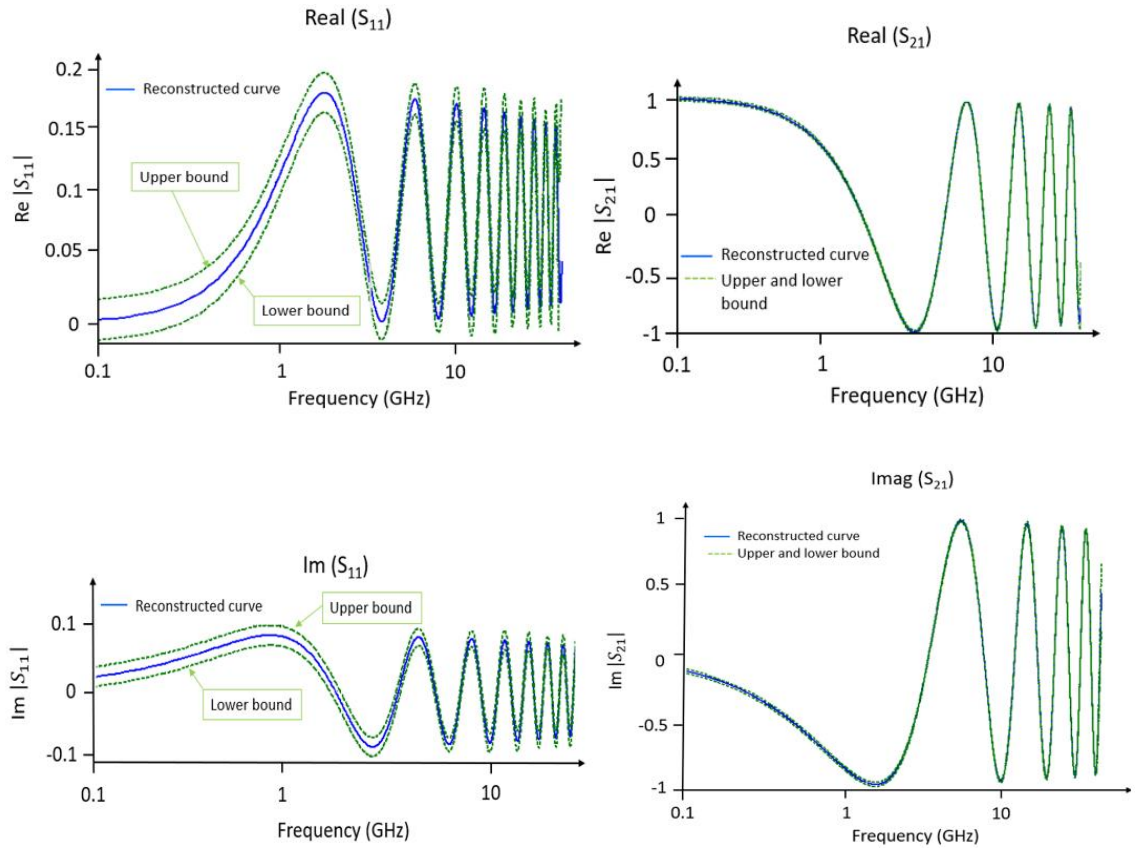

Fig. 2.18 Causality test applied to S_{11} and S_{21} for a line with characteristics: R_z = 3 um, w =230 um, and l = 25 mm.

As observed, no violations to causality occur, therefore, the reconstructed *S*-parameters from the causal model passes the requirement for causality.

2.3 Conclusions

In this chapter, the proposed methodology for incorporating the effect of the conductor surface roughness into the modeling of the attenuation and phase delay of PCB lines is described. The procedure includes the parameter extraction of the roughness feature parameter R_z, using a quadratic regression of data. Once this parameter is obtained, the implementation of a causal model that describes the surface roughness is carried out by calculating the conductor and dielectric contributions presented in the attenuation and phase delay propagation features. These results are afterwards validated by frequency and time domain simulations. The results obtained here are also checked for causality compliance. Furthermore, the following specific results were verified:

- The roughness presented between the conductor and the dielectric layers, not only affects directly the attenuation, it also impacts the phase delay. Here, it was verified that β is affected in two different ways: in the increase of the internal inductance inside the conductor, and also changing the capacitance and the effective permittivity of the microstrip dielectric environment including air and the PCB laminate.

- The R_z parameter, necessary for the implementation of a causal model, was obtained using a quadratic regression, omitting the use of optical measurements as in other approaches.

- A separation of the contributions of the conductor and dielectric materials including the surface roughness effect, was successfully carried out.

- The characteristic impedance was calculated under three different scenarios: when a causal model is used, when a non-causal assumption is considered, and when the phase delay is not considered ($K_\beta = 0$). A noticeable difference is shown in the real part of the characteristic impedance.

- A good agreement was shown between the measured *S*-parameters with the reconstruction of the *S*-parameters when the causal model was considered.

- Validations in the frequency and time domains as well as a test for causality of the reconstructed *S*-parameters were carried out successfully.

CHAPTER 3

APPLICATION OF THE SURFACE ROUGHNESS MODEL WITHIN THE W-BAND

In the previous chapter, a new methodology for taking into consideration the effect of the surface roughness on the electrical response of microstrip lines on PCB technology was presented. The relevance of a contribution of this type relies on the wide use of microstrip technology not only for designing data links or any other interconnects, but also other devices built using this technology. Actually, many of the most important components in microwave electronics are implemented on PCB to achieve cost-effective circuits: filters, power splitters, and antennas, just to mention a few examples. Among these components, research on PCB antennas is increasingly drawing attention due to the wide range of applications where they are essential. For instance, microstrip antennas are key elements in radar systems for automobiles, where these devices are operating within the W-band (75 – 110 GHz). Hence, this chapter is dedicated to analyze the performance of these components including the impact of the conductor finite roughness. For this purpose, the modeling approach proposed in this doctoral project shows usefulness. In fact, it is demonstrated that the physically meaningful representation of the several effects influencing the electrical features of antennas allows identifying the bottleneck limiting the associated performance.

What follows points out the practical relevance of the research conducted in this project; the developed methodologies are applied to exhaustively analyze the electrical characteristics of patch antennas built on PCB microstrip technology. The results are used to quantify the variation in the antenna's response from ideal design conditions due to the conductor surface roughness and lack of isotropy of the PCB dielectric laminate.

3.1 Microstrip patch antenna

With the emergence of 5G and 6G communications, mobile devices required high bandwidths and data rates. For this reason, patch antennas have become very popular as they present several advantages in addition to their electrical performance, like low costs, ease of manufacturing, and light weight [31]. Furthermore, their compatibility with PCB technology and microwave circuits has motivated extensive research on these devices. In fact, some of the figures of merit used to characterize patch antennas are: resonant frequency, bandwidth, gain, efficiency, shape of the radiation pattern, input impedance, among others [31]. All these parameters are strongly dependent on the properties of their constituent materials. For illustration purposes, a systematic procedure to assess the impact of imperfections of these materials on the resonant frequency of microstrip patch antennas is presented in this chapter.

3.1.1 Structure for a microstrip antenna

Microstrip patch antennas consist of a planar rectangular conducting shape called 'patch' mounted on a dielectric substrate, as shown in Fig. 3.1(a). Commonly, a microstrip line used to feed the antenna is included as an inset to the patch antenna, which is necessary to apply signals, but may substantially limit the overall performance of the device. For reference, in Fig. 3.1(a), the corresponding dimensions are shown: the length L and width W, which are complemented by the height h given by the substrate thickness. In addition, in Fig. 3.1(b), the top view of the antenna is depicted, where D is indicated, which is the length of the inset, and s is the microstrip-to-patch gap.

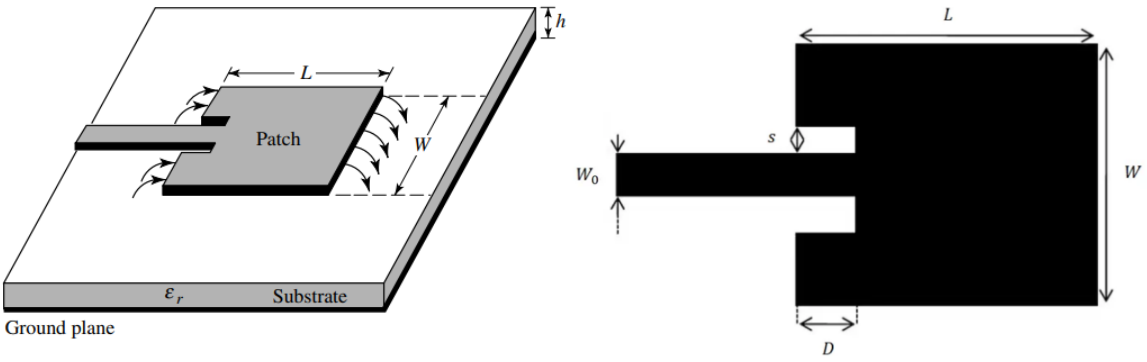

(a) (b)

Fig. 3.1 Sketches of a microstrip patch antenna: (a) a 3D perspective of the antenna [32], and (b) a top view where the main dimensions are indicated.

3.1.2 Idealized design equations

Designers typically use traditional textbook formulas to determine the dimensions of antennas for a particular application. These formulas are approximations that neglect high order effects that take importance at microwave frequencies, such as that of the metal surface roughness. Hence, to understand the impact of these assumptions on the calculations, the simple design equations are briefly discussed afterwards.

For a patch antenna, the dimensions can be calculated while considering the desired resonant frequency. In this case, the width of the patch antenna is calculated as [33]:

$$W = \frac{\lambda_0}{2}\left(\frac{2}{\varepsilon_r + 1}\right)^{1/2} \tag{3.2}$$

where λ_0 is the free-space wavelength of the signal at the resonant frequency (f_r), and ε_r is the relative permittivity of the dielectric substrate alone, whereas L is defined as:

$$L = \frac{c}{2f_r\sqrt{\varepsilon_{eff}}} - 0.824h\left(\frac{(\varepsilon_{eff} + 0.3)(W/h\ + 0.264)}{(\varepsilon_{eff} - 0.258)(W/h + 0.8)}\right) \tag{3.3}$$

In this equation, c is the speed of light, and ε_{eff} is the effective permittivity.

On the other hand, for the case of D, the design equation is given by [34]:

$$D = \frac{L}{\pi}\cos^{-1}\left(\sqrt[4]{\frac{Z_{feedline}}{Z_{antenna}}}\right) \tag{3.1}$$

where $Z_{feedline}$ is the impedance of the microstrip line, and $Z_{antenna}$ is the impedance of the antenna. Typically, s is determined for a specific frequency and considering given substrate properties from synthesis formulas found in antenna design books.

Since part of the waves propagating through any microstrip structure travel in the dielectric substrate and part in the air, an effective dielectric constant ε_{eff} is experienced by the signals, which can be approximately obtained from a quasi-static analysis from:

$$\varepsilon_{eff} = \frac{\varepsilon_r + 1}{2} + \frac{\varepsilon_r - 1}{2}\left[\frac{1}{\sqrt{1 + 12\left(\frac{h}{W}\right)}}\right] \tag{3.4}$$

Furthermore, because fiberglass reinforced laminates are used in practical PCBs, the effective permittivity depends on the orientation of the lines with respect to the fiber yarns. Therefore, an appropriate selection of the dielectric materials accounting for the tightness of the fibers to achieve a desired homogeneity must be carried out. This topic will be key on the study of the performance of the patch antennas since notice that consideration of neither the substrate inhomogeneity nor the surface roughness effects is made on the presented design equations.

3.1.3 Input impedance

A patch antenna is a one-port device; thus, electrically it only can be analyzed from its input impedance, which is obtained from VNA measurements. In this case, the S_{11} parameter or reflection coefficient Γ is related to the input impedance, Z_{in}; considering that the VNA has been previously calibrated and a reference impedance $Z_{ref} = 50\ \Omega$ is defined, the following equation relates Z_{in} and Γ:

$$S_{11} = \Gamma = \frac{Z_{in} - Z_{ref}}{Z_{in} + Z_{ref}} \tag{3.5}$$

Since the characterization of antennas presented in this work is based on measurements of Γ, equation (3.5) will be used to analyze experimental data associated to the impedance of multiple patch antennas in the following sections.

3.1.4 Selection of dielectric materials

When selecting a laminate material for high speed/frequency antenna design, the composite material properties critically determine whether or not the antenna patches and interconnects meet the application requirements. Therefore, it is important to consider that the laminate is fabricated with a combination of fiber glass impregnated with epoxy resins [35]. For this reason, the inhomogeneity of the materials may be experienced by the propagating signals. This is commonly known as the fiber weave effect and introduces variations in the permittivity and loss tangent, depending on the location of the interconnect; these variations become relevant when the wavelength of the harmonic of the maximum operation frequency approaches the size of the windows formed by the woven PCB fabrics. Consequently, a careful selection of the conductor and dielectric materials is necessary when working with high frequency applications.

3.2 Separation of the microscale effects present in antennas

Two main microscale effects related to the materials occur in practical microwave circuits: the fiber weave effect influencing the permittivity and the loss tangent, and the conductor surface roughness [36], as revised in the previous chapter. Therefore, when analyzing high-frequency antennas, a separation of the dielectric and conductor related effects is necessary to comprehend the corresponding impact on the electrical performance of antennas. For this purpose, to appropriately contribute to this investigation, two advanced laminate materials identified as 2136 and 2137 were selected to fabricate prototypes to support the analysis experimentally. In this regard, the 2136 material was constructed with a low permittivity resin matrix reinforced with woven fibers, whereas the 2137 material was constructed with an equally low permittivity resin matrix but without a woven fiber reinforcement. Hence, the 2137

exhibits homogeneity and it is expected that it presents less variations in the effective permittivity experienced by the signals.

3.2.1 Antenna and microstrip prototypes and measurements

To evaluate the performance of microstrip patch antennas in inhomogeneous materials, microstrip lines and patch antennas operating in the W-band for 5G and 6G applications, were considered. Since these structures were fabricated on two different materials, as previously explained, two coupons of the same material were designed to contain the following structures, where the angles are measured with respect to the fiber yarns:

- 4 sets of microstrip lines of 5, 15, and 30 mm long with orientations at 0°, 3°, 7°, and 10°.
- 2 sets of patch antennas fed with a 5 mm microstrip lines and oriented at 0°, 3°, 7°, and 10°.
- 2 sets of patch antennas fed with a 10 mm microstrip lines and oriented at 0°, 3°, 7°, and 10°.

These orientations were chosen based on the knowledge that routing angles smaller than or equal to 10° are the most prone to originate the resonances, as explained in [36]. To better illustrate the structures, Fig. 3.2 is showing a sketch of the corresponding two coupons for each material.

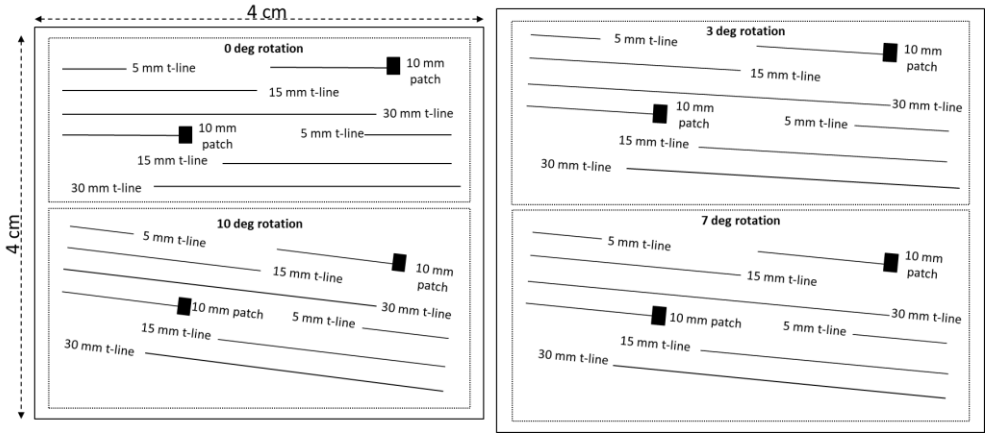

Fig. 3.2 Layout of the fabricated coupons showing the different microstrip lines and the patch antennas to be analyzed.

Furthermore, the electrical characteristics and some dimensions of the laminates are presented in Table 3.1, while the physical dimensions of the microstrip lines and the patch antennas are shown in Fig. 3.3. It is important to mention that the 0.32-mm width of the microstrip lines allows achieving a 50-ohm impedance, while the dimensions of the patch antennas yield a resonant frequency of 81 GHz.

Table 3.1 Characteristics of the selected dielectric laminates.

Material	Reinforced with woven fiber	Substrate height	Roughness profile (R_z)	Conductor thickness	ε_r @40GHz	tanδ @40GHz
2136	Yes	127 µm	0.88 µm	15.88 µm	3	0.0012
2137	No	127 µm	0.88 µm	15.88 µm	2.98	0.0013

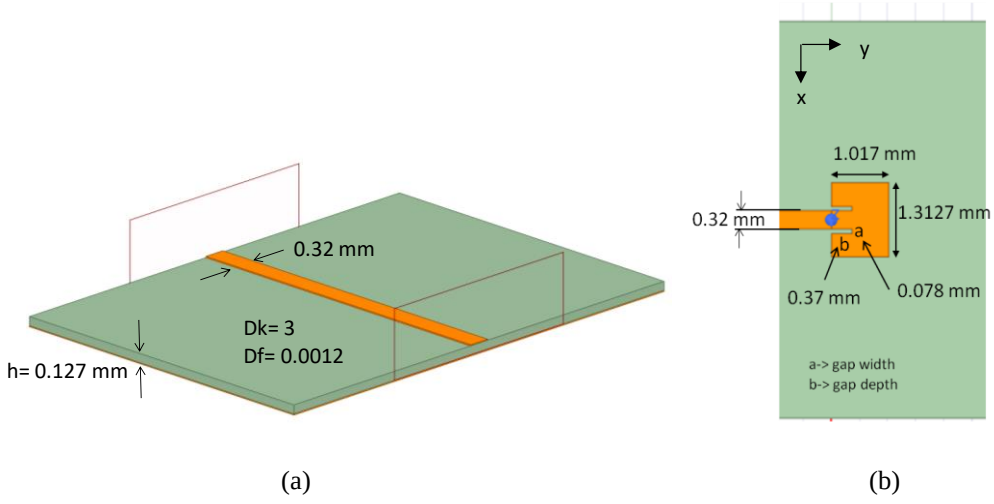

(a) (b)

Fig. 3.3 Details of the dimensions for the structures of the: (a) microstrip lines, and (b) patch antennas.

On the other hand, a verification of the physical dimensions was carried out for the microstrip lines once fabricated through a visual inspection. In this manner, the cross-section image was obtained to confirm that the values established in the design stage did not suffer from significant variation after the fabrication procedure. For this reason, Fig. 3.4(a) shows the cross-section of one of the microstrip lines, while in Fig. 3.4(b) a table with the details of the corresponding dimensions for the microstrip are shown.

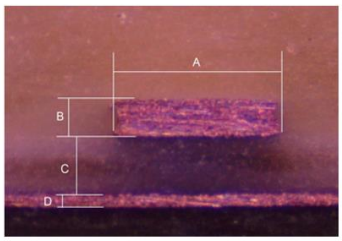

Cross-section results		2136 dimensions (µm)	2137 dimensions (µm)
A	Trace width	330	302
B	Trace thickness	88	107
C	Dielectric thickness	113	102
D	Gnd plane thickness	25	29

(a) (b)

Fig. 3.4 Details of the cross-section of the microstrip lines for the two considered laminates, where (a) presents a photograph of the cross-section, and (b) shows the calculated dimensions from (a).

After this validation, electrical measurements were performed in the High-Frequency Laboratory of INAOE to obtain the *S*-parameters of the microstrip lines, as well as the one-port reflection coefficient of the antennas. Since both structures are terminated with ground-signal-ground (GSG) pads, coplanar RF probes were used with a pitch of 250 µm to perform the measurements. To illustrate this, Fig. 3.5 provides photographs taken during the procedure. The setup included a VNA arrangement for measurements up to 100 GHz, with a calibration of the VNA using the line-reflect-reflect-match (LRRM) algorithm and an impedance-standard-substrate (ISS) of 50 Ω provided by the manufacturer.

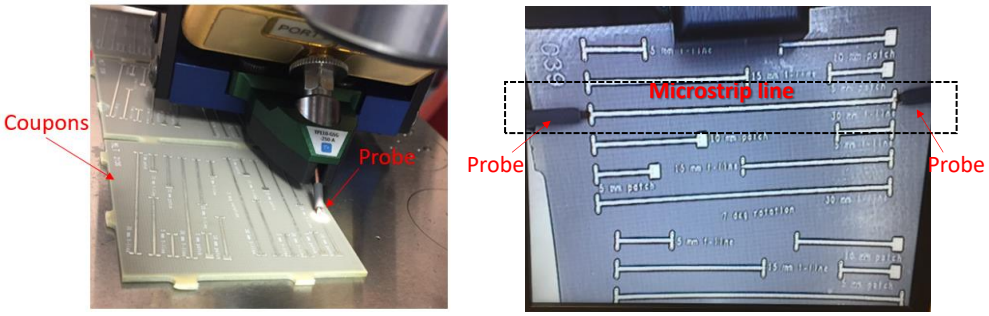

(a) (b)

Fig. 3.5 Photographs illustrating: (a) measurements of the antennas, and (b) measurements of the microstrip line.

After performing the measurements, the *S*-parameters of the microstrip lines were obtained and the line-to-line algorithm was applied to extract the propagation constant (γ) [20], which includes the information of the attenuation and phase delay considering the surface roughness effect.

3.2.2 Electromagnetic simulations

It is important to remark that the resonant frequency is affected by the speed of electromagnetic waves in a microstrip environment, which is in turn dependent upon the effective permittivity experienced by the propagating signals. Therefore, an assessment of the effects on the resonant frequency from varying the permittivity and loss tangent, was carried out. With this purpose, EM simulations in HFSS were performed using the corresponding models illustrated in Fig. 3.3.

During the simulation-based analysis presented in this section, the effect of the microstrip line used to feed the patch antenna was removed by shifting the input waveguide port close to the patch through de-embedding; this allowed for a performance analysis of the microstrip patch alone. To begin the parametric analysis, $\tan\delta$ was maintained at the nominal value of 0.0012 and four simulations considering variations in ε_r were carried out. The values for this parametric study were selected to define two ranges: i) two values of ε_r that represent lower and upper limits slightly beyond the expected range practical for a high-performance material, and ii) two additional ε_r values that define a wider range where a significant impact on the performance of the antennas can be observed. Consequently, for case i), ε_r = 2.85 and 3.15 were selected, and for case ii), ε_r = 2.5 and 3.5 were selected.

In Fig. 3.6, the resonant frequency $f_r \approx 81$ GHz was obtained by considering the nominal value of ε_r used as reference to compare the resonance variations observed in cases i) $f_r \approx 78.8$ GHz and ii) 82.3 GHz. These variations of ε_r ±0.15 are beyond the typical limits established by PCB manufacturers for advanced materials. For illustration purposes only, we further exaggerated these variations to show that significant changes in ε_r may require considerable re-sizing of the patches. This example is shown in Fig. 3.6, where plots corresponding to ε_r variations of ±0.5 are included.

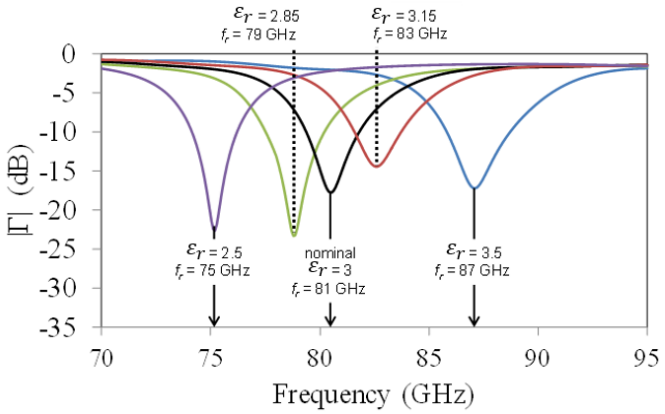

Fig. 3.6 EM simulations comparing the response of patch antennas reflecting variations on ε_r while maintaining $tan\delta$ = 0.0012 (i.e., nominal value).

For a second set of EM simulations, the ε_r parameter was fixed at 3 and variations of tanδ around the nominal value were performed. The resulting curves are shown in Fig. 3.7. Marginal changes are observed in the resonance frequency when tanδ varies from 0.0008 to 0.0016, which points out the stronger dependence of f_r on ε_r rather than on tanδ when considering variations of the dielectric loss beyond reasonable limits expected in actual PCB implementations.

It is important to emphasize that the resonance shift to lower frequencies is an expected trend when tanδ is increased. In fact, this effect can be better distinguished when considering much larger variations on tanδ as in [37]. However, that analysis only considered the impact of changes in ε_r and tanδ on the performance of the patch alone. Increasing the dielectric loss would have an impact on the microstrip line used to feed the patch, which was separately analyzed before.

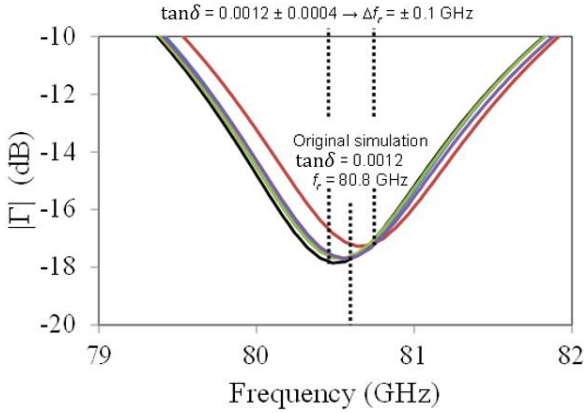

Fig. 3.7 EM simulations comparing the response of patch antennas reflecting variations on $tan\delta$ while maintaining ε_r = 3 (i.e., the nominal value).

The fluctuations in the antenna radiation pattern were also investigated. In Fig. 3.8 and Fig. 3.9, the radiation patterns of the simulated models with variations in ε_r and $\tan\delta$, respectively, are presented. As clearly shown, the radiation power at far field is barely modified for the E and H planes (Phi = 90° and 0°, respectively). Nevertheless, as expected for the variations in ε_r, the pattern is significantly affected. However, the variations near the nominal specifications seemed to not impinge greatly on the antenna performance.

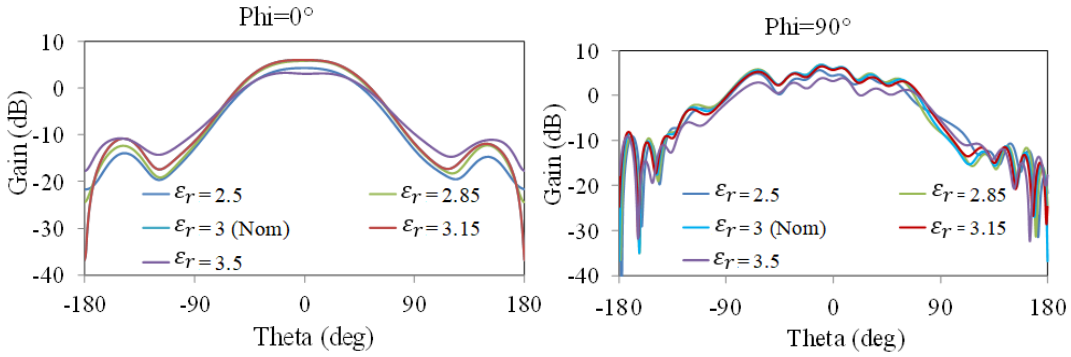

Fig. 3.8 EM simulation results showing radiation patterns for Phi = 90° and 0° (E and H planes) with variations in ε_r.

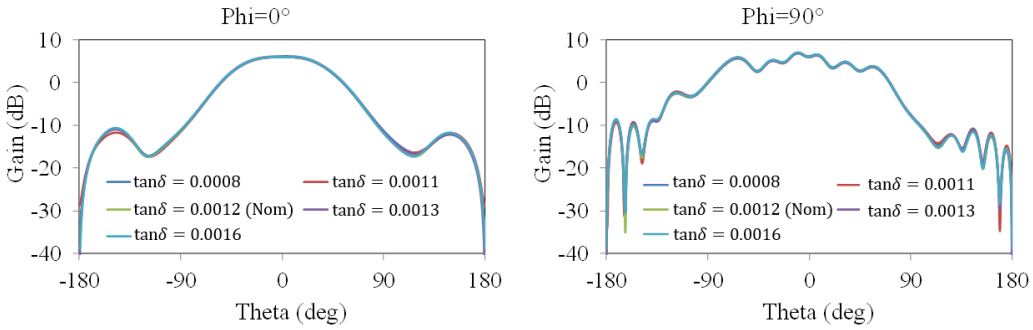

Fig. 3.9 EM simulation results showing radiation patterns for Phi=90° and 0° (E and H planes) with variations in $tan\delta$.

3.2.3 Parameter extraction

To start modeling the microstrip lines present in the fabricated PCB coupons considering the roughness effect, the methodology for the model used in Chapter 2 was applied. Once having the corresponding value of the roughness exhibited by the conductor, an EM simulation in HFSS was carried out considering this effect in the layer between the conductor and the dielectric materials. Afterwards, the permittivity of the dielectric was considered dependent on frequency and represented by the Debye model [38]. Then, a 2D EM simulation of the line's

cross section was used to extract the ε_r and $\tan\delta$ associated with only the dielectric laminate. The corresponding results are shown in Fig. 3.10 for the 2136 laminate, and in Fig. 3.11 for the 2137 laminate. Observe that the variation in these parameters with the tracing angle are well below the ranges considered during the parametric simulation analysis previously described, which suggests that small variations are also present in the measured resonant frequencies due to tolerances in the dielectric laminate properties.

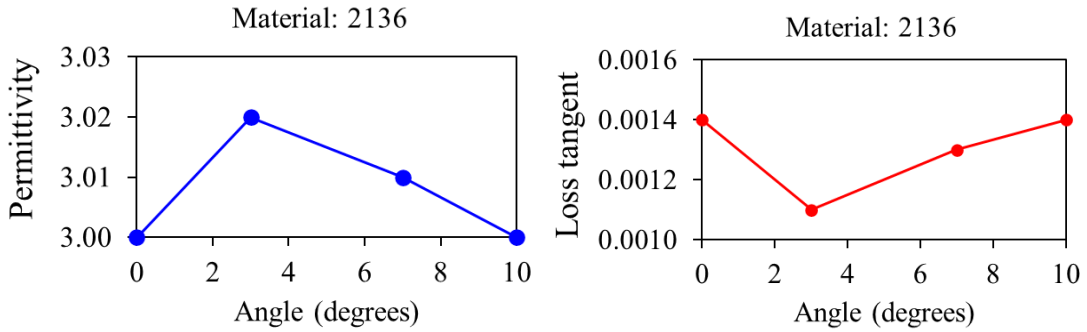

(a) (b)

Fig. 3.10 Values obtained for the (a) permittivity, and (b) loss tangent for the laminate 2136.

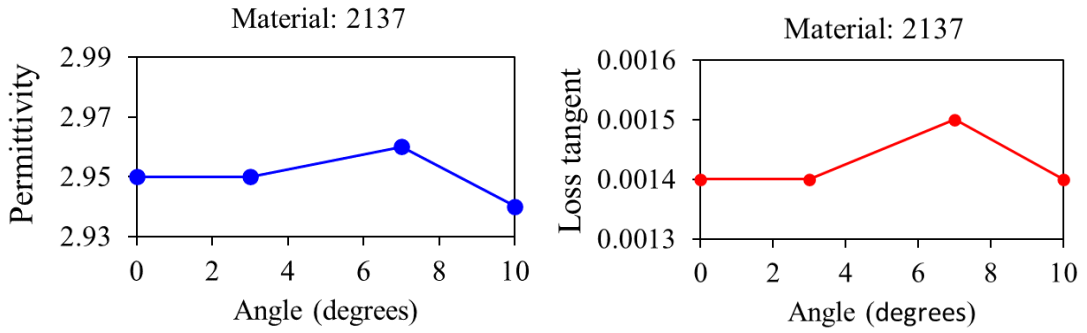

(a) (b)

Fig. 3.11 Values obtained for the (a) permittivity, and (b) loss tangent for the laminate 2137.

As expected, marginal variation for the laminate 2137 are shown, since this is the material that exhibits homogeneity.

3.3 Impact of the fiber weave effect in the performance of antennas

To experimentally verify the hypothesis that the resonant frequency may also vary depending on the antenna orientation, a direct inspection of the path antenna reflection coefficient data without the effect of the signal launch and feeding lines was carried out to quantify the limitations of the patch itself [39]. Nonetheless, removing the parasitic effects introduced by the electrical transitions occurring from the probes to the patch was difficult, since there are no practical means to independently measure each section of the patch test structure [40]. To further illustrate the followed procedure, the four sections considered in the equivalent circuit model are shown in Fig. 3.12, where the C_{in} and L_{in} parameters account for the pad parasitics, and C_{tran} and L_{tran} represent the discontinuity between the microstrip line (physical length, characteristic impedance, γ) and the patch. As demonstrated in [41], redundancies can be employed to determine C_{in}, L_{in}, C_{tran}, and L_{tran}.

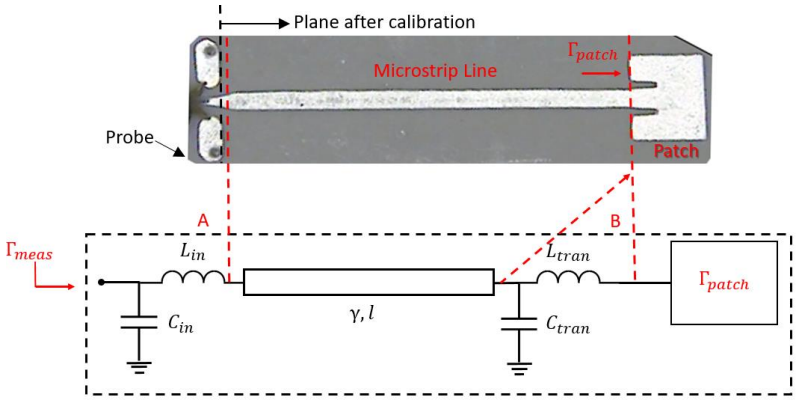

Fig. 3.12 Test-fixture for measuring the patch antenna.

In the prototypes, patch antennas were included featuring microstrip feeding lines of two different lengths (i.e., 5 mm and 10 mm). Since the patches were assumed to exhibit negligible variation in their characteristics when traced at the same angle, both structures were expected to radiate signals at the same resonant frequency. Therefore, given the equivalent circuit rendered in Fig. 3.12, γ and l are known, and the characteristic impedance of the microstrip can be computed [42]. Next, the circuit in Fig. 3.13 was implemented in a circuit simulator considering reflection coefficient data measured from two patch antennas. In Fig. 3.12 and 3.13, Γ_{meas} and Γ_{patch} represent the experimental reflection coefficient before and after de-embedding, respectively. Hence, the inductors and capacitors associated with the transitions

are obtained by correlating Γ_{patch} for the two patches at the same angle, but fed by microstrip lines of different length. While performing this procedure, it was necessary to assume that the values for C_{in}, L_{in}, C_{tran}, and L_{tran} remain the same for the two patch antenna structures. Furthermore, to simplify the procedure, C_{in} and L_{in} were obtained in advance from measurements performed on the microstrip lines traced at the same angle as the patches [41].

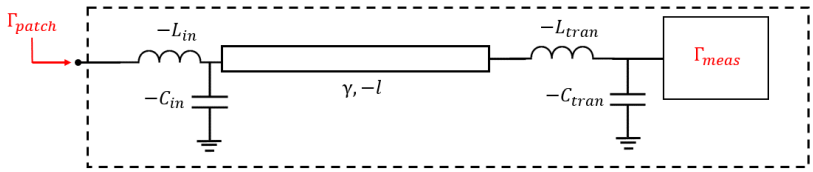

Fig. 3.13 De-embedded circuit for the patch antenna.

The results obtained for Γ_{patch} are shown in Fig. 3.14 for patch antennas traced at 0°. Noticeably, the resonant frequencies are in agreement for patches of the same size and orientation, even though the de-embedded feeding line exhibited different lengths. Hence, this procedure was applied to all the patch antenna measurements to observe the variations in the resonance frequency with respect to the tracing angles.

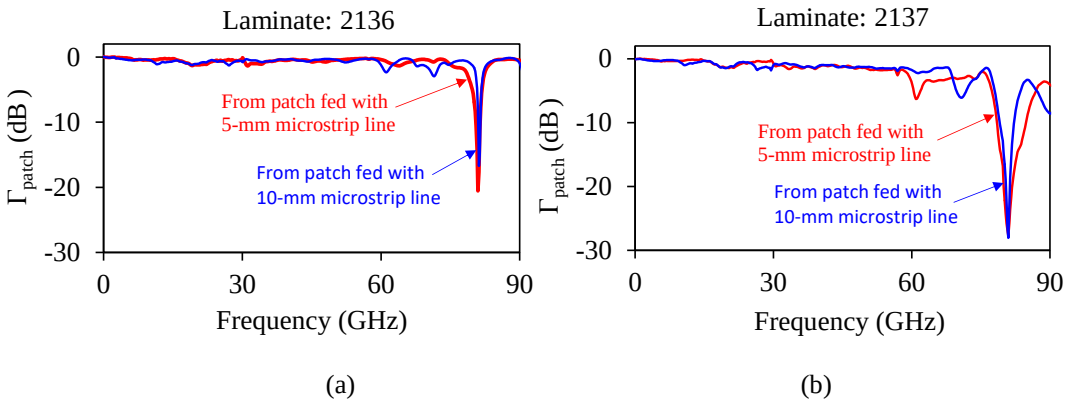

Fig. 3.14 Γ_{patch} for two patches traced at 0° on materials: a) 2136, and b) 2137. Effects of transition between probe and path are de-embedded from these results.

Finally, Fig. 3.15 shows the de-embedded reflection coefficient corresponding to antennas traced at different angles for the two considered materials. Observe that barely noticeable differences in this parameter were obtained from the experiments, which confirms that both laminates were effectively used to achieve the target operating frequency of the patch antennas. In fact, plotting the resonant frequencies for both antennas at all routing angles, shows that the variation was marginal as depicted in Fig. 3.16.

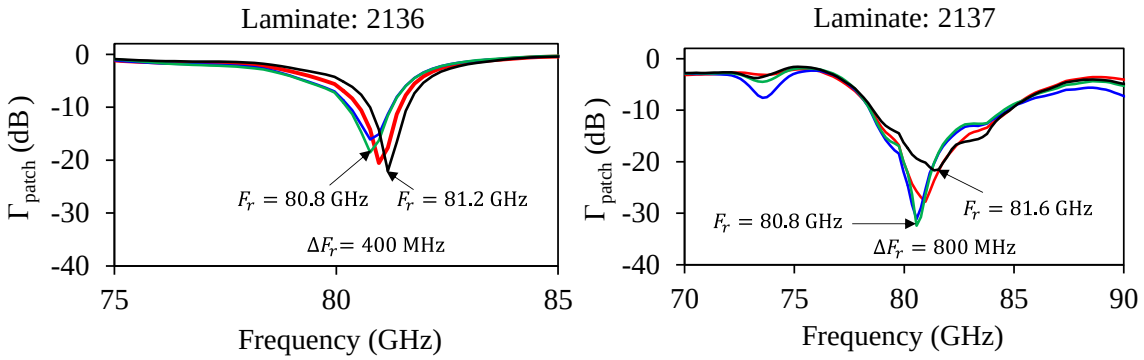

(a) (b)

Fig. 3.15 Reflection coefficient showing the resonant frequency for: (a) laminate 2136, and (b) laminate 2137.

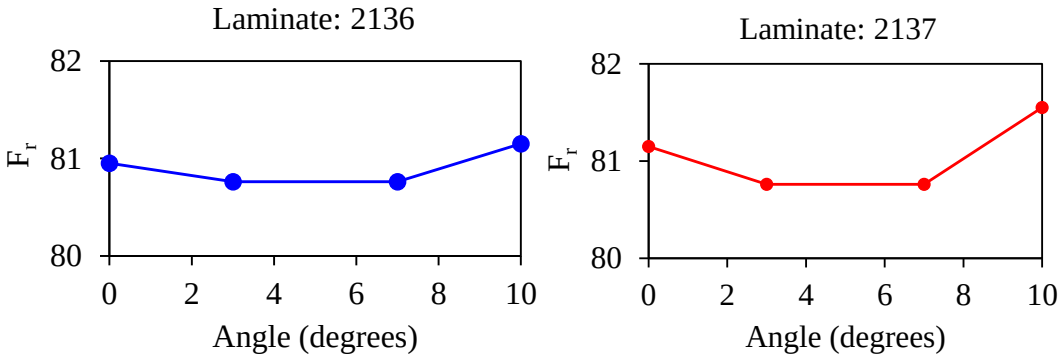

(a) (b)

Fig. 3.16 Resonant frequency versus angle plots for: (a) laminate 2136, and (b) laminate 2137.

3.4 Conclusions

An application of the modeling methodology for the conductor surface roughness effect, was demonstrated by experimentally analyzing several sets of patch antennas built in two different prototypes. Since one of the dielectric laminates serving as substrates for the antenna devices are made with fiber reinforced resins, variations on the electrical performance were identified by considering different conductor tracing angles. This analysis was possible only because the systematic separation of conductor and dielectric effects was achieved by characterizing separately the loss and delay introduced by the conductor and dielectric media through which the applied signals travel.

CHAPTER FOUR

INCORPORATING THE SURFACE ROUGHNESS EFFECT IN THE MODELING OF SUBSTRATE INTEGRATED WAVEGUIDES

The modeling methodology for microstrip lines operating at microwave frequencies has been presented and applied to analyze not only lines but also patch antennas. Nevertheless, it is worthwhile remarking the fact that the effect incorporated to the corresponding models is based on an additional loss and delay, which are introduced by the scattering of waves with the imperfect conductor surface. Bear in mind, however, that this effect is also observed in conductor structures used to guide signals in propagation modes differing from the TEM or quasi-TEM. For this reason, this chapter describes how the modeling approach developed in this thesis can be extended to other types of waveguides and propagation modes. In fact, due to its importance on current PCB microwave technology, the selected waveguide to demonstrate this fact is the synthetic rectangular waveguide, also known as the PCB substrate integrated waveguide (SIW).

SIWs are widely used at microwave frequencies due to their compatibility with PCB technology [43] within several applications [44]–[46]. This allows for implementing from interconnects [47], to resonators for determining material properties [48]–[51]. Therefore, to achieve the full characterization of a uniform section of SIW propagating in single mode, accurate knowledge of the complex propagation constant (γ), and the wave impedance (Z_{wave}) is necessary. In fact, once these fundamental parameters are known, the properties of the constituting dielectric and conductor materials can be inferred [52], the effect of the SIW when used as an access component can be de-embedded [53], and even equivalent circuit models can be implemented to represent the signal propagation when using the structure in a practical circuit [54],[55].

Whereas γ can be obtained by the line-to-line formulation from S-parameter measurements, obtaining Z_{wave} is cumbersome due to the difficulty of accounting for the combined dielectric and conductor effects occurring in practical SIWs [56]. For this reason, rather than neglecting losses at all, as in simplified formulations for rectangular waveguides

(RWGs) [13],[57], using the data corresponding to the complex γ for calculating Z_{wave} is recommended.

Therefore, as part of the characterization methodologies proposed in this thesis, in this chapter, Z_{wave} is obtained from experimental γ data assuming propagation in the dominant TE_{10} mode. For this purpose, a new parameter extraction methodology is presented for considering the conductor losses including the effect of the finite roughness of the metal foils required to form the waveguide. To achieve this, simple electromagnetic (EM) simulations are employed to support the parameter extraction. Moreover, as part of the characterization for the SIW, a causal model for the complex relative dielectric permittivity (ε_r) is implemented, which also allows for characterizing the dielectric properties of the laminate used as PCB substrate from SIW measurements. Once Z_{wave} is determined, the power-current, voltage-current, and power-voltage impedances (i.e., Z_{pi}, Z_{vi} and Z_{pv}, respectively) can be directly obtained depending on the desired description for the SIW. In fact, processing γ and Z_{wave} allows for obtaining the frequency-dependent per-unit-length (P.U.L.) resistance, inductance, conductance, and capacitance (*RLGC*) elements of the SIW to identify the difference in the curves when common simplifications are applied.

4.1 Approaches used for the determination of Z_{wave}

By assuming the dominant TE_{10} propagation mode, as in typical cases where SIWs guide signals on PCB [5], Z_{wave} can be calculated from $\gamma = \alpha + j\beta$ data using the following equation, which is expanded here in real and imaginary parts [58]:

$$Z_{wave} = \frac{\omega\mu_0}{\beta} + j\frac{\omega\alpha\mu_0}{\beta^2} \tag{4.1}$$

where assuming that the fields propagate in a lossless magnetic medium, the permeability of vacuum (μ_0) is used. However, since the magnetic field also interacts with the conductor material, a complex permeability is experienced by the traveling waves. Moreover, even though approaches considering non-ideal conductor effects provide good results for air-filled waveguides [59], substantial errors are introduced for SIWs built even with low-loss PCB dielectric materials. Alternatively, transmission line models can be applied to indirectly obtain Z_{wave} [54]. Nevertheless, accounting for the additional loss introduced by the conductor

roughness requires accurate knowledge of the surface topography [60], which is not always possible in practical scenarios.

4.2 Relationship between γ and Z_{wave}

This section is dedicated to establish a relationship that allows to obtain Z_{wave} from γ assuming that single TE_{10} propagation mode is taking place. Therefore, assuming transmission line theory, it is possible to arrive to the well-known generic *RLGC* model, shown in Fig. 4.1(a) and to its modified version, shown in Fig. 4.1(b), for the TE_{10} propagation mode.

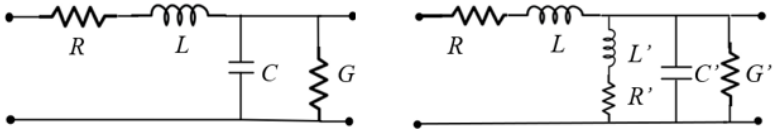

(a) (b)

Fig. 4.1 Equivalent circuit models for a transmission line, where (a) is the common circuit model, and (b) is the modified version [54].

Besides, since *R* and *L* exhibit no variation between these two models, Z_{wave} can be expressed as [61]:

$$Z_{wave} = \frac{R + j\omega L}{\gamma} \tag{4.2}$$

where *R* and *L* are respectively given by [54]:

$$R = 1/\delta\sigma h \tag{4.3}$$

$$L = \mu_0 + \frac{R}{\omega} \tag{4.4}$$

In (4.3), *h* is the height of the RWG parallel to the electric field, σ is the conductivity of the metal, and the skin depth is:

$$\delta = \sqrt{1/\pi\sigma\mu_0 f} \tag{4.5}$$

In (4.2), *R* represents the loss effects due to longitudinal currents along the top and bottom walls of the waveguide, while the term R/ω in (4.4) corresponds to an inductance component also internal to the conductor. Hence, these two effects can be accounted for in the calculation of Z_{wave}.

4.2.1 Development of a new expression for Z_{wave}

In this thesis, it is proposed a new expression for Z_{wave} that can be obtained by substituting (4.4) into (4.2) to yield:

$$Z_{wave} = \frac{\omega\mu_0\beta + R(\alpha+\beta)}{\alpha^2+\beta^2} + j\frac{\omega\mu_0\alpha - R\beta + R\alpha}{\alpha^2+\beta^2} \tag{4.6}$$

Furthermore, considering that the waveguide is made of PCB low-loss dielectric materials, and copper, it is reasonable to assume at microwave frequencies that $\alpha^2 \ll \beta^2$, $R(\alpha+\beta) \ll \omega\mu_0\beta$, and $R\alpha \ll (\omega\mu\alpha - R\beta)$, which allows obtaining the following simplified equations from (4.6):

$$\mathrm{Re}(Z_{wave}) \approx \frac{\omega\mu_0}{\beta} \tag{4.7}$$

$$\mathrm{Im}(Z_{wave}) \approx \frac{\omega\mu_0\alpha - R\beta}{\beta^2} \tag{4.8}$$

In this case, it was observed that (4.7) corresponds to the real part of Z_{wave} also obtained from (4.1), which is the approximation used in practice. This is due to its accurate representation of $\mathrm{Re}(Z_{wave})$, illustrated hereafter by simulating a uniform section of waveguide exhibiting the cross section depicted in the inset of Fig. 4.2(a), which presents a cutoff frequency of the TE_{10} mode, $f_{TE10} \approx 27$ GHz. This EM simulation is performed using Ansys HFSS that also allows to directly obtain the complex Z_{wave} from the excitation waveguide port. In Fig. 4.2(a), the real part of this simulated Z_{wave} is compared with the curve calculated from the simulated β using (4.7); excellent correlation is achieved. Conversely, when comparing the imaginary part of the simulated Z_{wave} with the calculation using (4.1), significant discrepancy is observed in Fig. 4.2(b). It is also shown in this figure, that using the approximation for a hollow RWG given in [59] is not appropriate when there exist dielectric losses. In contrast, the curves obtained using the simulated β and (4.8) provide an accurate representation of $\mathrm{Im}(Z_{wave})$ even when rough conductors are assumed by employing Huray's model during the simulations [11]. In this case, a nodule radius $n_r = 0.5$ μm, and the Hall-Huray surface ratio $SR = 3$ were used for representing a standard copper profile.

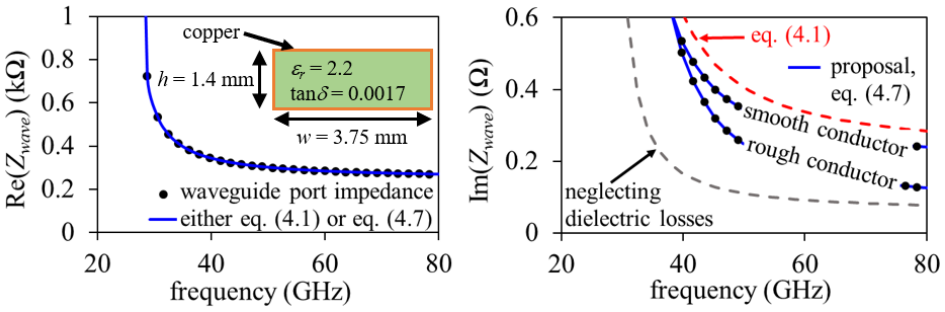

(a) (b)

Fig. 4.2 Zwave obtained from EM simulated data, applying different equations, and compared with the port impedance directly provided by the simulation software: (a) real part, and (b) imaginary part. The inset shows the details of the simulated RWG.

Hence, as can be seen in (4.8), accounting for the conductor effects in the imaginary part requires considering the $R\beta$ term. Since $\beta = \mathrm{Im}(\gamma)$ can easily be obtained from experiments, the strategy to obtain R is explained later in this thesis.

4.3 Prototypes and experiments

To experimentally corroborate the proposal, two SIW prototypes were built by considering two different widths (w_1 = 4.1 mm, and w_2 = 2.3 mm) and to different lengths (l_1 = 76.2 mm, and l_2 = 254 mm). The SIWs were designed to exhibit a cutoff frequency of $f_{TE10} \approx 27$ GHz, and $f_{TE10} \approx 47$ GHz, for the lines with w_1 and w_2, respectively. Furthermore, the structures were designed to excite only odd propagation modes, so the next excited mode after TE_{10} is the TE_{30} becoming apparent above 80 GHz. On the other hand, the dielectric laminate has a thickness h = 1.4 mm and a nominal relative permittivity of $\varepsilon_r = 2.2$ [62]. The center-to-center separation and the diameter of the vias are $s = 0.69$ mm and $d = 0.48$ mm, respectively. To illustrate the prototypes used, Fig. 4.3 shows photographs of the SIWs, as well as some of their dimensions.

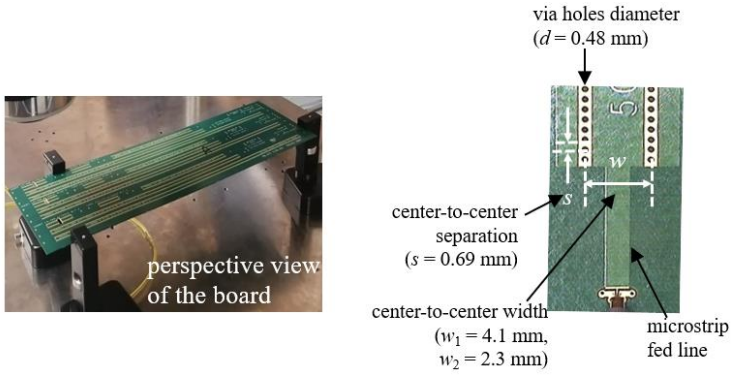

(a) (b)

Fig. 4.3 Pictures of the SIW prototypes showing: (a) a perspective view of the board containing the SIWs, and (b) the dimensions of the prototypes used.

These structures presented microstrip feed lines and pads to land probes with a pitch of 250 µm, which allows measuring the *S*-parameters. Before this procedure, the VNA was calibrated to shift the measurement plane up to the end of the probes using the line-reflect-reflect-match (LRRM) algorithm. Afterwards, *S*-parameters were obtained up to 80 GHz, before exciting the TE_{30} propagation mode.

4.4 Parameter extraction

To obtain Z_{wave} using the proposed equation (4.8), *R* must be firstly determined. Hence, even though this resistance can be obtained from calculations considering the effective dimensions and conductor material properties as in [54], the effect of the surface roughness would be neglected. Thus, an improved approach was proposed in [60], but requiring information about the metal surface topography [63]. This involves the measurement of the surface roughness, which are not always possible in practice once the prototype is built. For this reason, an alternative parameter extraction procedure is explained afterwards.

At tens of gigahertz, the skin depth is so small that the effect of the internal conductor inductance on β is negligible. Therefore, the real part of the complex relative permittivity (i.e., $\varepsilon_r = \mathrm{Re}(\hat{\varepsilon}_r)$) is obtained from [64]:

$$\varepsilon_r' = \frac{\beta^2 + \left(\frac{\pi}{w_{eff}}\right)^2}{\omega^2 \mu_0 \varepsilon_0} \tag{4.9}$$

where $w_{eff} = w - d^2/0.95s$ is the effective width of the SIW [65], and ε_0 is the vacuum permittivity. Since ε_r' and $\tan\delta$ are linked through causality, Djordjevic's model can be implemented to obtained these parameters in the SIW frequency range. For the modeling of the real part of the permittivity, the next equation is employed [66]:

$$\varepsilon_r' = \varepsilon_\infty + \frac{\Delta\varepsilon'}{m_a - m_b} \frac{\ln\left|\frac{f_b + jf}{f_a + jf}\right|}{\ln 10} \tag{4.10}$$

where ε_∞ is the real part of ε_r' at high frequencies, f_1 and f_2 are respectively the lower and upper limits of the f range for the experimental ε_r', $\Delta\varepsilon' = \varepsilon_r'(f_a) - \varepsilon_r'(f_b)$, and $m_1 = \log(f_a)$ and $m_2 = \log(f_b)$. Defining these parameters allow the simultaneous determination of the model for the two considered widths. Later, ε_r'' is obtained to follow the calculation for $\tan\delta$ by using [66]:

$$\varepsilon'' = \frac{\Delta\varepsilon'}{m_a - m_b} \frac{\arg\left(\frac{f_b + jf}{f_a + jf}\right)}{\ln 10} \tag{4.11}$$

Therefore, $\tan\delta$ is calculated as:

$$\tan\delta = \frac{\varepsilon''}{\varepsilon'} \tag{4.12}$$

In this manner, Fig. 4.4 shows the results for ε_r' and $\tan\delta$ when Djordjevic's causal model is applied to the SIW.

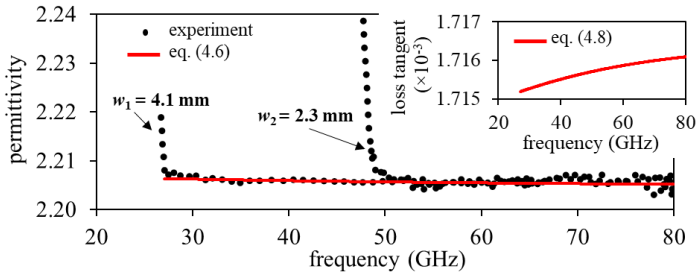

Fig. 4.4 Curves of the determination of the permittivity and loss tangent using Debye's causal model.

At this point, it is important to remark that the dielectric properties of the PCB laminate have been obtained from SIW measurements.

4.4.1 EM simulations

The next step is to calculate R for applying (4.8) to an SIW on PCB, where R including the effect of the copper roughness is necessary [67]. In this case, R is associated to the longitudinal current along the SIW and thus suffers from the additional loss introduced by the surface roughness effect on the top and bottom walls. Therefore, R_{rough}, which includes the surface roughness effect can be represented using [68]:

$$R_{\text{rough}} = K_{\text{H}} \times R_{\text{smooth}} \tag{4.13}$$

where K_{H} is the roughness correction factor, which can be obtained from EM simulations in HFSS of a uniform section of SIW with a width w_1 = 4.1 mm, exhibiting the additional dimensions shown in Fig. 4.3, and defining the frequency dependent permittivity and loss tangent of the dielectric material using the already implemented models given by (4.10)–(4.12).

For the simulation, Huray's model was used to represent the losses introduced by the finite roughness of the top and bottom copper walls. In this case, through a model–experiment correlation involving the attenuation data corresponding to the SIW, the associated Huray's model parameters defined in HFSS are found to be n_r = 0.5 μm and SR = 2.9. Fig. 4.5(a) shows the agreement between the model and the experimental α. From this simulation, the complex $\gamma_{\text{rough}}^{\text{EM}}$ and $Z_{\text{wave\_rough}}^{\text{EM}}$ are determined, where the 'EM' superscript and the 'rough' subscript are used to indicate that these parameters are obtained from EM simulation and considering rough surfaces, respectively. Through this simulation, R_{rough} can be obtained from $\gamma_{\text{rough}}^{\text{EM}}$ and $Z_{\text{wave\_rough}}^{\text{EM}}$ as:

$$R_{\text{rough}} = \text{Re}\left(\gamma_{\text{rough}}^{\text{EM}} \times Z_{\text{wave\_rough}}^{\text{EM}}\right) \tag{4.14}$$

And the K_H factor can now be obtained from (4.13) as:

$$K_H = R_{\text{rough}}/R_{\text{smooth}} \tag{4.15}$$

where R_{smooth} is obtained from (4.3). Moreover, a Simonovich's causal model for the roughness correction factor can be implemented to represent the results from (4.13). The mathematical form of this model is rewritten hereafter [17]:

$$K_{H\_\text{model}} = 1 + \frac{(\Delta K - 1)c_x f}{c_x f + \sqrt{2c_x f} + 1} \tag{4.16}$$

where the pyramidal array of spheres described in Chapter 2 was assumed, yielding $\Delta K = 8.33$. Besides, using the methodology proposed in this thesis and also described in Chapter 2, $c_x = 2.64\times10^{11}$ is obtained, which depends on material properties and on R_q. In this case, the correlation for obtaining this later parameter involves the equation given by (4.16) and data computed from (4.15). This is shown in Fig. 4.5(b).

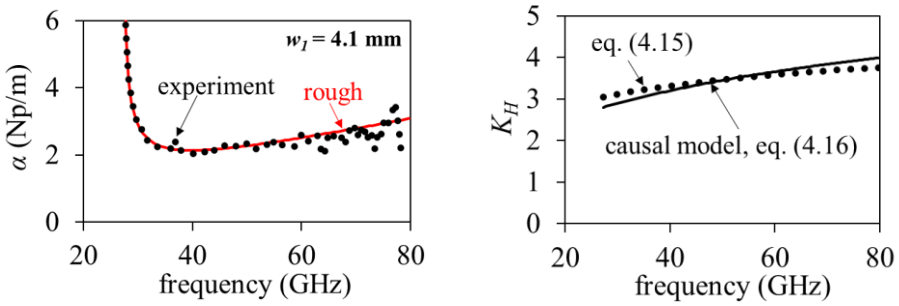

Fig. 4.5 Illustration of the determination of the factor K_H: (a) correlation of α curves obtained through an EM simulation including the metal surface roughness and from measurements, and (b) data calculated for K_H and represented using a causal model.

In conclusion, either equation (4.15) using results from simulations, or applying directly a causal model for the conductor roughness (i.e., eq. (4.16)), allows for obtaining the correction factor K_H.

4.4 Tests and validations

Now (4.7) and (4.8) can be validated using the SIW prototypes since R containing the surface roughness effect has been included. Therefore, Fig. 4.6 and Fig. 4.7 shows the complex wave impedance for a SIW of w_1 = 4.1 mm, and w_2 = 2.3 mm, respectively. It can be observed that either (4.1) or (4.7), represent well the real part of Z_{wave}. While the imaginary part clearly differs when considering (4.8) or other approximations.

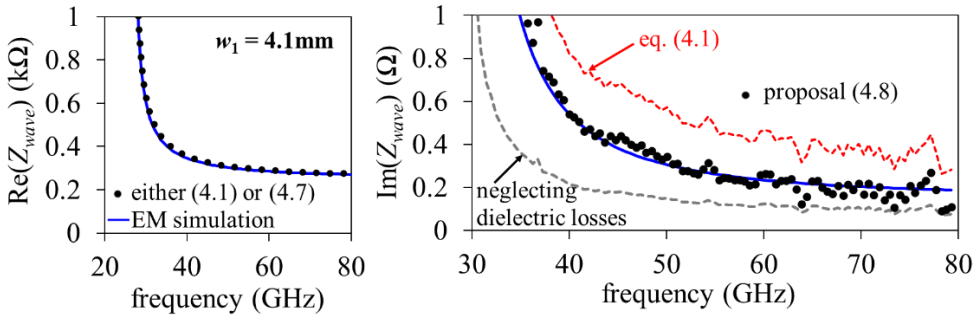

(a) (b)

Fig. 4.6 Z_{wave} curves from different approaches: (a) real part, and (b) imaginary part, for a SIW of w_1 = 4.1 mm.

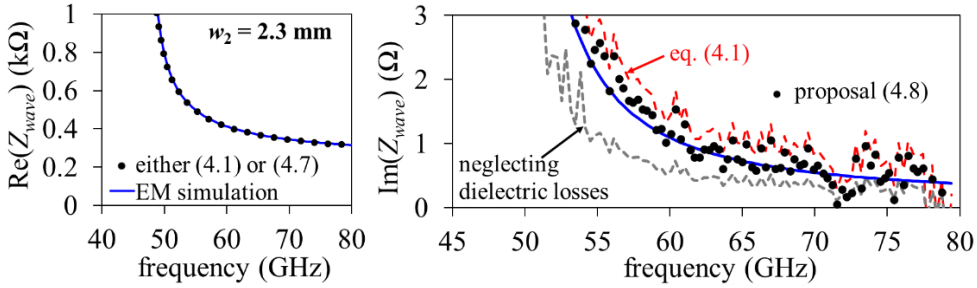

(a) (b)

Fig. 4.7 Z_{wave} curves from different approaches: (a) real part, and (b) imaginary part, for a SIW of w_1 = 2.3 mm.

Again, it is observed that the $R\beta$-term plays an important role to properly described the losses related to the materials, especially when accounting for the surface roughness effect as well.

To demonstrate the application of the proposed model for Z_{wave}, the curves for equivalent circuit model elements in Fig. 4.1(b) are obtained versus frequency using the following equations:

$$R = \mathrm{Re}(\gamma \times Z_{wave}) \tag{4.17}$$

$$L = \mathrm{Im}(\gamma \times Z_{wave})/\omega \tag{4.18}$$

$$G' = \omega \varepsilon_0 \varepsilon_r \tan\delta \tag{4.19}$$

$$C' = \varepsilon_0 \varepsilon_r \tag{4.20}$$

$$Y_{RL} = \frac{\gamma}{Z_{wave}} - G' - j\omega C' \tag{4.21}$$

$$R' = \mathrm{Re}\left(\frac{1}{Y_{RL}}\right) \tag{4.22}$$

$$L' = \mathrm{Im}\left(\frac{1}{Y_{RL}}\right)/\omega \tag{4.23}$$

Where Y_{RL} is the shunt admittance associated with the series connection of R' and L'. Thus, when using the experimentally determined data for γ, ε_r and tanδ, in the previous equations, the curves shown in Fig. 4.8 are obtained for the circuit elements that represent the losses occurring in the SIW. In all cases, correlation is observed with EM simulations performed using the 3D model for the SIW in HFSS. In contrast, unexpected curve trends for *R* and *G*' are obtained when neglecting the dielectric losses in the calculation of Z_{wave}: *R* is clearly overestimated while *G*' drops with frequency. Likewise, ignoring the longitudinal currents in the top and bottom walls when obtaining this impedance as in (4.1) yields *R* = 0, whereas *R*' shows also an overestimation of the resistive effect associated to the transverse currents, which is predicted to be small by the EM simulation.

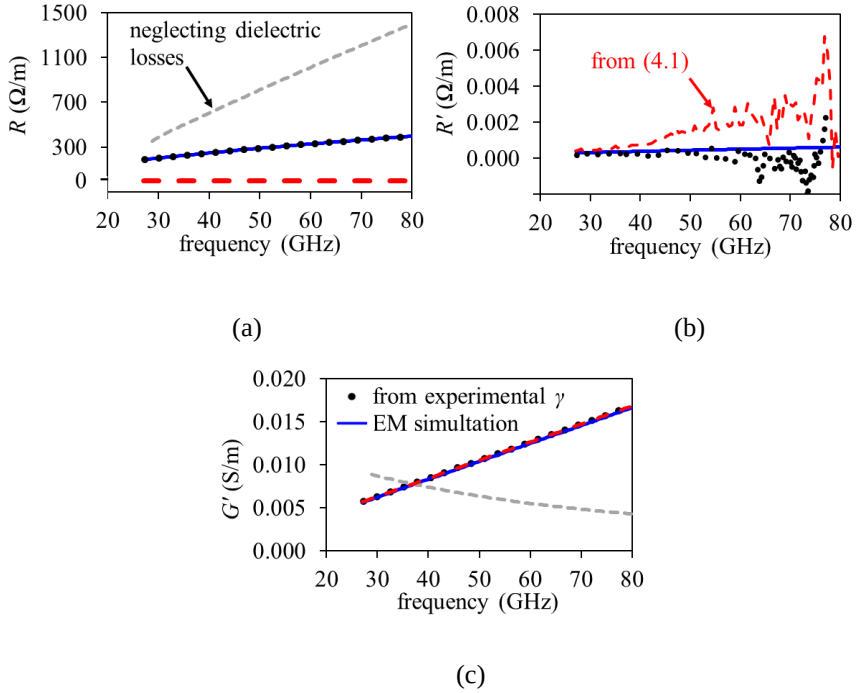

Fig. 4.8 Curves of the circuit elements: (a) *R*, (b) *R'*, and (c) *G'* which represent the loss effects. Cases are also showing other approximations.

As a final verification, *S*-parameters were reconstructed by using γ and Z_{wave}, and a length of *l* = 15 mm. This reconstruction was calculated by using firstly the following equation for obtaining the *ABCD* parameters:

$$\mathbf{T} = \begin{bmatrix} \cosh(\gamma l) & Z_{wave}\sinh(\gamma l) \\ Z_{wave}^{-1}\sinh(\gamma l) & \cosh(\gamma l) \end{bmatrix} \tag{4.24}$$

Afterwards, an *ABCD* to *S*-parameter transformation is performed by considering Z_{wave} as the reference impedance. This allows assuming that perfect matching occurs at the SIW terminations and the signal transmission is maximized. Hence, the model can be directly

assessed through analyzing the insertion loss (i.e., $|S_{21}|$). Fig. 4.9(a) shows that the reconstructed magnitude and phase for S_{21} corresponding to the uniform section of SIW agrees with the EM simulations. Furthermore, using (4.17)–(4.23) and the models for Z_{wave}, and the complex permittivity it is possible to obtain the circuit elements to simulate the insertion loss of the SIW. The corresponding curves also show agreement for the SIWs of the two considered widths as can be seen in Fig. 9(a) and Fig. 9(b). This verifies the applicability of the proposal to implement circuit models once Z_{wave} or its scaled versions (i.e., Z_{pi}, Z_{vi} and Z_{pv}) are determined.

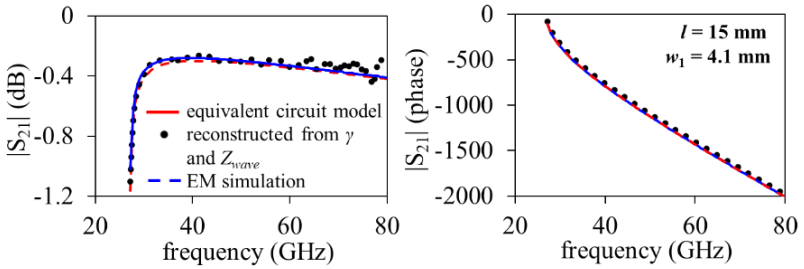

(a)

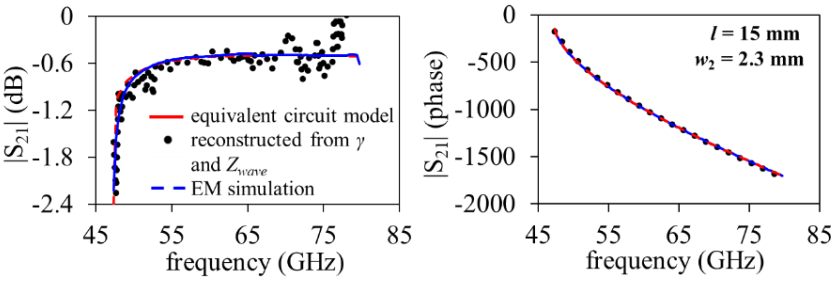

(b)

Fig. 4.9 Curves of the circuit elements: (a) *R*, (b) *R'*, and (c) *G'* which represent the losses. Also showing other approximations.

4.5 Conclusions

The surface roughness effect associated to the conductor forming an SIW was analytically incorporated into the propagation model. Furthermore, this allows the indirect determination of the corresponding wave impedance in a straightforward manner. This was achieved by proposing a new expression for obtaining the complex wave impedance of an SIW functioning in the TE_{10} propagation mode. This mathematical representation has been validated by an excellent correlation of simulations with data measured to SIW varying in width and up to 80 GHz. Moreover, provided that the single-mode propagation is fulfilled, this approach can easily be extended to other structures and higher frequencies.

CHAPTER FIVE

GENERAL CONCLUSIONS

This project was dedicated to enable the physical representation of the metal surface roughness effect on the propagation features of microwave interconnects. Why complying with causality is mandatory to achieve the accurate modeling used in both the frequency and time domains in a consistent fashion was described in detail. For this reason, the complex roughness coefficient was described and for the first time a methodology for representing its frequency dependent parts was presented. Furthermore, it was pointed out the importance of considering not only the attenuation due to conductor effects but also the delay, specially at frequencies near the lower limit of the microwave range.

5.1 Implementation of a causal model for conductor surface roughness

The methodology presented in Chapter 2 consisted in a parameter extraction to obtain the effective peak-to-valley feature R_z, which describes the roughness profile. Once this parameter was obtained, both the attenuation and delay introduced by the conductor effects are accurately represented and verified up to 30 GHz for lines operating in the quasi-transverse electromagnetic mode. These results were afterwards validated with optical measurements performed independently. Furthermore, time and frequency domain simulations and a check for causality compliance were carried out to verified the modeling. Therefore, in this thesis was presented for the first time as a new and straightforward model parameter determination methodology, assuming that the roughness parameter R_z is unknown.

5.1.1 Remarks on the modeling approach

The methodology proposed in this thesis finds application from two different perspectives. The first one is that of the technology developers, which manufacture, optimize, and provide the

specifications for the electrical performance of copper foils. On the other hand, from a circuit designer perspective, knowing the figures-of-merit of a copper foil allows to evaluating its pertinence for a certain application, as well as implementing causal models for circuit simulations.

Certainly, the prototypes used exhibit characteristics needed to avoid significantly complicating the analysis. Thus, as for many practical cases in electronics, it is recommended building a prototype specifically for modeling the electrical effects introduced by the conductor roughness. In this regard, lines of different lengths are needed. Moreover, to reduce uncertainty in assessing this conductor-related effect, dielectric loss effects should be maintained low. For this reason, using thin and low-loss dielectric laminates is desirable for the prototype, whereas avoiding including solder mask is recommended. Bear in mind that, once this electrically-obtained R_z feature is known for a foil with a given profile, the model for the surface impedance can be implemented. This complements the representation of a practical interconnect when using this foil to form either, the signal trace or the ground plane.

Finally, it is not the intention of this proposal to substitute imaging-based analyses performed to inspect the detailed topology of copper foils, which is important, for instance to analyze its adhesion properties. Rather, its contribution is providing a parameter extraction that takes advantage of the average interaction of microwave signals with microscopic protuberances to provide means for the electrical representation of the surface roughness effect.

5.2 Assessment in the performance of antennas for 5G/6G applications

Due to the relevance of the surface roughness effect at microwave frequencies, in this project it was also demonstrated the application of the new modeling methodology for carrying out the full analysis of the electrical features of antennas operating within the W-band. It is worthwhile mentioning that applying available simplifications rather than the proposal, yield overestimation of the delay and loss introduced by the dielectric environment. This may even lead to misinterpreting measured results and incorrectly concluding that improving the characteristics of the laminates that serve as substrate allow avoiding the additional delay and loss that is originated in the metallic structures.

For this purpose, patch antenna devices were fabricated in the microstrip technology where the lack of isotropy in the dielectric laminate is considered. Additionally, the roughness effect on the conductor foil is also exhibited in the prototypes. Since there where two microscale effects involved, it was necessary to firstly isolate the surface roughness effect and then perform the study of the impact of the fiber weave effect presented in the laminates. Once this procedure was completed, variations in the electrical propagation were expected as the laminates suffer from the fiber weave effect. However, the results suggested minor differences in the permittivity and in the loss tangent for both laminates Additionally, the resonant frequency was also observed according to the location of the antenna. All of these parameters concluded that both materials were adequate for the antennas and its application. The reason of this result is that both of the analyzed materials were intended for microwave applications. Nevertheless, the importance of analyzing these two cases was the fact that one of the materials still uses reinforced glass fibers. Thus, provided that the yarns are closely spaced, a laminate like this exhibits properties similar to those built without reinforcement.

5.2.1 Important aspects about the impact in the performance of patch antennas

When observing the resonant frequency according to the orientation, the antennas routed on 2136 material exhibited ~0.17 standard deviation from target resonance frequency, while the antennas routed on 2137 material using the exact same antenna configuration, exhibited ~0.21 standard deviation from target mean frequency. This implies that the 2136 material composite of low loss resin matrix and low permittivity woven glass fiber offers optimal ‘homogeneous’ behavior compared to an equivalent advanced non-woven fiber reinforced material. Furthermore, the extraction of the permittivity values conducted on microstrip lines routed on both materials resulted in a 1.34 % and a 1.37 % change for the 2136 and 2137 materials, respectively. These percentage values were calculated when compared to the datasheet values specification. Therefore, the data obtained from this investigation thus far concludes that inhomogeneous advanced copper clad laminate materials exhibit characteristics that are suitable for W-band antenna designs.

5.3 Modeling extension to substrate integrated waveguides

Finally, it was also demonstrated here that the modeling of the roughness effect is relevant for interconnects propagating signals in modes different from the quasi-TEM. For instance, in rectangular waveguides, which find wide applications at tens of gigahertz and are candidates to substitute current electrical interconnections on conventional PCBs. This served as a motivation to dedicate effort in this project to develop the theory for synthetic RWGs such as SIWs. In this regard, it was even identified how the surface roughness effect becomes important to define the characteristic impedance of the waveguide. For this reason, a new expression to explicitly indicate this effect in the mathematical definition of the wave impedance of a SIW was proposed. Among the advantages of this new formulation, it is worthwhile mentioning that finds usefulness to characterize the properties of the materials forming the waveguide, and to develop equivalent circuits that allow for their electrical representation in circuit simulators.

This expression included the conductor and dielectric losses, as well as the losses due to the surface roughness effect. No other approximations available in literature consider these three types of losses in substrate integrated waveguides in a simple form. The proposal was validated through experiments and by using electromagnetic simulations. The results showed good agreement with the proposed equation.

5.3.1 Physical interpretation of the expression for Z_{wave} proposed

In this thesis, the following expression for Z_{wave} was proposed in Chapter 4:

$$Z_{wave} \approx \frac{\omega\mu_0}{\beta} + \frac{\omega\mu_0\alpha - R\beta}{\beta^2} \tag{5.1}$$

This expression considers all loss and delay effects occurring in the SIW structure since α and β are influenced by the EM wave interactions within the dielectric, and the conductor materials, including for instance those at the sidewalls. The novelty of (5.1) is that the influence of R is explicitly indicated in the numerators of the real and imaginary parts. Also, from (5.1) can be noticed that the expression is very similar to previous formulations already published, however in here, the $R\beta/\beta^2$-term is due to the current propagation in the SIW, where:

- *R* associated to the longitudinal currents, which corresponds to the losses occurring in the top and bottom plates of the SIW, whereas
- *R*' is associated to the transversal currents, which includes the vias of the SIW

This new equation for Z_{wave} was validated by applying it for two different widths for the SIWs, however, this can be easily extended when the physical dimensions are changed. Furthermore, once the wave impedance is obtained, other impedance definitions can be used, for instance, to aid in the implementation of equivalent circuit models for the SIW when used as interconnect or as part of more complicated circuits.

References

[1] T. Sieber, *What is Moore's Law and is it still relevant in 2023?* [Online]. Available: https://www.makeuseof.com/tag/what-is-moores-law-and-what-does-it-have-to-do-with-you-makeuseof-explains/

[2] D. M. Cortés Hernández, (2017), *Modeling of microwave transmission lines considering frequency-dependent current distribution effects*, PhD thesis, Instituto Nacional de Astrofísica, Óptica y Electrónica.

[3] H. Johnson and M. Graham, *High-Speed Signal Propagation. Advanced Black Magic*. Hoboken, NJ, USA: Prentice Hall, 2003.

[4] C. L. Holloway and G. A. Hufford, "Internal inductance and conductor loss associated with the ground plane of a microstrip line," *IEEE Trans. Electromagn. Compat.*, vol. 39, no. 2, pp. 73–78, May 1997, doi: 10.1109/15.584929.

[5] G. R. Luevano, T. Michalka, V. Sonawane, and V. Sriboonlue, "Copper roughness induced gain for inductance and resistance on stripline interconnects," in *Proc. IEEE Int. Symp. Electromagn. Compat. Signal/Power Integr.,* Spokane, WA, USA, 2022, pp. 392–396, doi: 10.1109/EMCSI39492.2022.9889464.

[6] M. Cauwe and J. De Baets, "Broadband material parameter characterization for practical high-speed interconnects on printed circuit board," *IEEE Trans. Adv. Packag.*, vol. 31, no. 3, pp. 649–656, Aug. 2008, doi: 10.1109/TADVP.2008.927853.

[7] E. Hammerstad and O. Jensen, "Accurate models for microstrip computer-aided design," *IEEE MTT-S Int. Microw. Symp.*, Washington, DC, 1980, pp. 407-409.

[8] S. P. Morgan, "Effect of surface roughness on eddy current losses at microwave frequencies," *Journal of Applied Physics*, vol. 20, no. 4, pp.352–362, Apr 1949.

[9] G. Brist, S. Hall, S. Clouser, and T. Liang, "Non-classical conductor losses due to copper foil roughness and treatment," in *Proc. Electron. Circuits World Conv. 10*, Anaheim, CA, Feb., 2005.

[10] S. Hall *et al.*, "Multigigahertz causal transmission line modeling methodology using a 3-D hemispherical surface roughness approach," *IEEE Trans. Microw. Theory Tech.*, vol. 55, no. 12, pp. 2614–2624, Dec. 2007, doi: 10.1109/TMTT.2007.910076.

[11] P. G. Huray et al., "Fundamentals of a 3-D 'snowball' model for surface roughness power losses," *IEEE Electromagn. Compat.*, vol. 9, no. 2, pp. 62–65, 2nd Quarter 2020, doi: 10.1109/MEMC.2020.9133247.

[12] J. Coonrod, "The effect of radiation losses on high frequency PCB performance," in *Proc. IPC APEX EXPO*, 2014.

[13] D. M. Pozar, *Microwave Engineering*, 4th ed. New York, NY, USA: Wiley, 2012.

[14] L. Simonovich, “A practical method to model effective permittivity and phase delay due to conductor surface roughness”, in *Proc. DesignCon,* 2017.

[15] “Copper foils for high frequency materials”, Rogers Corporation, 2021.

[16] J. E. Bracken, “A causal Huray model for surface roughness”, in *Proc. DesignCon,* 2012.

[17] V. Dmitriev-Zdorov, L. Simonovich and I. Kochikov, “A causal conductor roughness model and its effect on transmission line characteristics,” in *Proc. DesignCon*, 2018.

[18] J. Coonrod, “Microwave radiation loss concerns in PCBs,” *The PCB Des. Mag*., pp. 32–34, Apr. 2013.

[19] *IEEE Standard for Precision Coaxial Connectors (DC to 110 GHz),* IEEE Standard 287, IEEE Instrumentation and Measurement Society, 2007.

[20] J. A. Reynoso-Hernandez, “Unified method for determining the complex propagation constant of reflecting and nonreflecting transmission lines,” *IEEE Microw. Wireless Compon. Lett*., vol. 13, no. 8, pp. 351–353, Aug. 2003, doi: 10.1109/LMWC.2003.815695.

[21] E. Y. Terán-Bahena, S. C. Sejas-García, and R. Torres-Torres, “Permittivity determination considering the metal surface roughness effect on the microstrip line series inductance and shunt capacitance,” *IEEE Trans. Microw. Theory Tech*., vol. 68, no. 6, pp. 2428–2434, Jun. 2020, doi: 10.1109/TMTT.2020.2979964.

[22] L. Simonovich, “A practical method to model effective permittivity and phase delay due to conductor surface roughness,” in *Proc. DesignCon,* 2017.

[23] A. F. Horn, P. A. Lafrance, C. J. Caisse, J. P. Coonrod, and B. B. Fitts, “Effect of conductor profile structure on propagation in transmission lines,” in *Proc. DesignCon,* 2016.

[24] S. H. Hall, G. W. Hall and J. A. McCall, *High-speed digital system design: a handbook of interconnect theory and design practices.* Hoboken, NJ, USA: Wiley, 2000.

[25] Y. Shlepnev, “Unified approach to interconnect conductor surface roughness modelling,” in *Proc. IEEE 26th Conf. Elect. Perform. Electron. Packag*. Syst., 2017, pp. 1–3, doi: 10.1109/EPEPS.2017.8329704.

[26] L. Simonovich, “Cannonball-Huray model demystified”, Lamsin Enterprises Inc., Issue 1, 2019, [Online]. Available: http://lamsimenterprises.com/WhitePaper_Cannonball-Huray%20Model%20Demystified.pdf

[27] A. F. Horn, J. W. Reynolds, P. A. Lafrance, and J. C. Rautio, “Effect of conductor profiles on the insertion loss, phase constant, and dispersion in thin high frequency transmission lines”, in *Proc. DesignCon*, 2010.

[28] D. Kaller et al., “Using S-parameters successfully in time domain link simulations,” in *Proc. IEEE 14th Topical Meeting Elect. Perform. Electron. Packag*., Austin, TX, USA, 2005, pp. 95–98, doi: 10.1109/EPEP.2005.1563710.

[29] P. Triverio and S. Grivet-Talocia, “Robust causality characterization via generalized dispersion relations,” *IEEE Trans. Adv. Packag*, vol. 31, no. 3, pp. 579–593, Aug. 2008, doi: 10.1109/TADVP.2008.927850.

[30] P. Triverio and S. Grivet-Talocia, “A robust causality verification tool for tabulated frequency data,” in *Proc. IEEE Workshop Signal Propag. Interconnects*, Berlin, Germany, 2006, pp. 65–68, doi: 10.1109/SPI.2006.289191.

[31] S. Verma, L. Mahajan, R. Kumar, H. S. Saini and N. Kumar, "A small microstrip patch antenna for future 5G applications," *5th International Conference on Reliability, Infocom Technologies and Optimization (Trends and Future Directions) (ICRITO),* Noida, India, 2016, pp. 460-463, doi: 10.1109/ICRITO.2016.7784999.

[32] C. A. Balanis, “*Antenna theory, analysis and design*”, 4th ed., John Wiley & Sons, Inc., Hoboken, 2016.

[33] R. Barman, S. Sinha, S. Roy, A. Das, “Design of inset feed microstrip patch antenna for Bluetooth application,” in *International Research Journal of Engineering and Technology (IRJET)*, Mar., 2017. Available online: https://www.irjet.net/archives/V4/i3/IRJET-V4I3623.pdf

[34] Z. Peterson, Microstrip patch antenna calculator for RF designers. [Online]. Available: https://resources.altium.com/p/microstrip-patch-antenna-calculator-rf-designers

[35] E. Y. Terán Bahena, (2019), Causal modeling and characterization of printed circuit board interconnects considering high-order effects in the microwave frequency range, PhD thesis, Instituto Nacional de Astrofísica, Óptica y Electrónica.

[36] G. Romo, R. Torres-Torres, S.-W. Baek, and M. Schauer, “Stack-up and routing optimization by understanding micro-scale PCB effects,” in *Proc. DesignCon*, 2011.

[37] M. M. Keskilammi, L.T. Sydanheimo, and M. A. Kivikoski, “Modeling electromagnetic wave propagation in paper reel for UHF RFID system development”, *Mechatronics for Safety, Security and Dependability in a New Era*, Elsevier, 2007, pp. 317−322.

[38] E. Moctezuma-Pascual, S. C. Sejas-García, and R. Torres-Torres, “Broadband determination of dielectric dissipation factor by implementing the multi-pole debye model through linear regressions”, in *Proc. DesignCon*, 2020.

[39] M. R. Karim, X. Yang and M. F. Shafique, “On chip antenna measurement: a survey of challenges and recent trends”, *IEEE Access*, vol. 6, pp. 20320−20333, 2018.

[40] W. Chouchene, C. Larbi, and T. Aguili, “New electrical equivalent circuit model of the inset fed rectangular patch antenna”, *Progress in Electromagnetics Research Symposium - Spring (PIERS)*, 2017, pp. 646−651.

[41] J.E. Post, “On determining the characteristic impedance of low-loss transmission lines”, *Microw. Opt. Technol. Lett*., vol. 47, pp 176−180, 2005.

[42] R. Torres-Torres, “Extracting characteristic impedance in low-loss substrates”, *Electronics Letters*, vol. 47, pp. 191−193, 2011.

[43] M. Bozzi, L. Perregrini and K. Wu, "Modeling of Radiation, Conductor, and Dielectric Losses in SIW Components by the BI-RME Method," in *Eur. Microw. Integr. Circuit Conf.*, Amsterdam, Netherlands, 2008, pp. te0–233, doi: 10.1109/EMICC.2008.4772271.

[44] Y. Shi, X. Yi, W. Feng, Y. Wu, Z. Yu and X. Qian, "77/79-GHz Forward-Wave Directional Coupler Component Based on Microstrip and SIW for FMCW Radar Application," *IEEE Trans. Compon. Packag. Manuf. Technol.*, vol. 10, no. 11, pp. 1879-1888, Nov. 2020, doi: 10.1109/TCPMT.2020.3031311.

[45] R. Y. Fang, C. F. Liu and C. L. Wang, "Compact and Broadband CB-CPW-to-SIW Transition Using Stepped-Impedance Resonator With 90 ∘ -Bent Slot," *IEEE Trans. Compon., Packag. Manuf. Technol.*, vol. 3, no. 2, pp. 247-252, Feb. 2013, doi: 10.1109/TCPMT.2012.2228306.

[46] J. N. Smith and T. Stander, "A Capacitive SIW Discontinuity for Impedance Matching," *IEEE Trans. Compon., Packag. Manuf. Technol.*, vol. 9, no. 11, pp. 2257-2266, Nov. 2019, doi: 10.1109/TCPMT.2019.2946945.

[47] J. J. Simpson, A. Taflove, J. A. Mix and H. Heck, "Substrate integrated waveguides optimized for ultrahigh-speed digital interconnects," *IEEE Trans. Microw. Theory Techn.*, vol. 54, no. 5, pp. 1983–1990, May 2006, doi: 10.1109/TMTT.2006.873622.

[48] M. Tlaxcalteco-Matus and R. Torres-Torres, “Modeling a SIW filter with IRIS windows using equivalent circuits,” *Microw. Opt. Technol. Lett.*, vol. 54, no. 12, pp. 2865–2868, 2006, doi: 10.1002/mop.27183

[49] L. Yan, W. Hong, G. Hua, J. Chen, K. Wu, and T. J. Cui, “Simulation and experiment on SIW slot array antennas,” *IEEE Microw. Wireless Compon. Lett.*, vol. 14, no. 9, pp. 446–448, Sep. 2004, doi: 10.1109/LMWC.2004.832081

[50] J.-X. Chen, W. Hong, Z.-C. Hao, H. Li, and K. Wu, “Development of a low cost microwave mixer using a broad-band substrate integrated waveguide (SIW) coupler,” *IEEE Microw. Wireless Compon. Lett.*, vol. 16, no. 2, pp. 84–86, Feb. 2006, doi: 10.1109/LMWC.2005.863199.

[51] J. W. Holloway, G. C. Dogiamis, S. Shin, and R. Han, “220-to-330-GHz manifold triplexer with wide stopband utilizing ridged substrate integrated waveguides,” *IEEE Trans. Microw. Theory Techn.*, vol. 68, no. 8, pp. 3428–3438, Aug. 2020, doi: 10.1109/TMTT.2020.2997367.

[52] Chao-Hsiung Tseng and Tah-Hsiung Chu, "Measurement of frequency-dependent equivalent width of substrate integrated waveguide," *IEEE Trans. Microw. Theory Techn.*, vol. 54, no. 4, pp. 1431–1437, June 2006, doi: 10.1109/TMTT.2006.871245.

[53] Q. -S. Wu and L. Zhu, "Numerical De-Embedding of Effective Wave Impedances of Substrate Integrated Waveguide with Varied Via-to-Via Spacings," *IEEE Microw. Wireless Compon. Lett.*, vol. 26, no. 1, pp. 1–3, Jan. 2016, doi: 10.1109/LMWC.2015.2505619.

[54] K. Lomakin, G. Gold, and K. Helmreich, "Transmission line model for rectangular waveguides accurately incorporating loss effects," in *Proc. 21st Workshop Signal Power Integrity (SPI)*, May 2017, pp. 1–4.

[55] G. Méndez-Jerónimo and K. Wu, "Effects of Unshielded Air Holes Periodically Perforated in Substrate Integrated Waveguides," *IEEE Microw. Wireless Compon. Lett.*, vol. 30, no. 11, pp. 1049–1052, Nov. 2020, doi: 10.1109/LMWC.2020.3022973.

[56] M. Bozzi, M. Pasian, L. Perregrini, and K. Wu, "On the losses in substrate-integrated waveguides and cavities," in *Int. J. Microw. Wireless Technol.*, pp. 395–401. doi:10.1017/S1759078709990493

[57] J. Helszajn, *Microwave Engineering: Passive, Active and Non-Reciprocal Circuits*, McGraw-Hill, 1991.

[58] N. Marcuvitz, *Waveguide Handbook*, 1986 Ed. Institution of Engineering and Technology, 1986.

[59] D. F. Williams, J. Jargon, U. Arz and P. Hale, "Rectangular-waveguide impedance," in *85th Microw. Measurement Conf. (ARFTG)*, Phoenix, AZ, USA, 2015, pp. 1–5, doi: 10.1109/ARFTG.2015.7162902.

[60] K. Lomakin, G. Gold, and K. Helmreich, "Analytical waveguide model precisely predicting loss and delay including surface roughness," *IEEE Trans. Microw. Theory Techn.*, vol. 66, no. 6, pp. 2649–2662, Jun. 2018, doi: 10.1109/TMTT.2018.2827383.

[61] R. B. Marks and D. F. Williams, "A general waveguide circuit theory," *J. Res. Nat. Instit. Standards Technol.*, vol. 97, no. 5, pp. 533–562, Sept.1992.

[62] Rogers Corporation, 2022, "RT/duroid® 5870/5880," Rogers Corporation.

[63] G. Gold and K. Helmreich, "A physical surface roughness model and its applications," *IEEE Trans. Microw. Theory Techn.*, vol. 65, no. 10, pp. 3720–3732, Oct. 2017, doi: 10.1109/TMTT.2017.2695192.

[64] M. D. Janezic and J. A. Jargon, "Complex permittivity determination from propagation constant measurements," *IEEE Microw. Guided Wave Lett.*, vol. 9, no. 2, pp. 76–78, Feb. 1999, doi: 10.1109/75.755052.

[65] Y. Cassivi, L. Perregrini, P. Arcioni, M. Bressan, K. Wu and G. Conciauro, "Dispersion characteristics of substrate integrated rectangular waveguide," *IEEE Microw. Wireless Compon. Lett.*, vol. 12, no. 9, pp. 333–335, Sept. 2002, doi: 10.1109/LMWC.2002.803188.

[66] A. R. Djordjevic, R. M. Biljie, V. D. Likar-Smiljanic, and T. K. Sarkar, "Wideband frequency-domain characterization of FR-4 and time domain causality," *IEEE Trans. Electromagn. Compat.*, vol. 43, no. 4, pp. 662–667, Nov. 2001, doi: 10.1109/15.974647

[67] M. Yi, et al., "Surface roughness modeling of substrate integrated waveguide in D-band", *IEEE Trans. Microw. Theory Techn*., vol. 64, no. 4, pp. 1209–1216, Apr. 2016, doi: 10.1109/TMTT.2016.2535290.

[68] Y. J. Cheng and X. L. Liu, “W-band characterizations of printed circuit board based on substrate integrated waveguide multi-resonator method,” *IEEE Trans. Microw. Theory Techn*., vol. 64, no. 2, pp. 599–606, Feb. 2016, doi: 10.1109/TMTT.2015.2511007.